

TOPICAL REVIEW

## Gas sensing devices based on two-dimensional materials: a review

To cite this article: Boran Wang *et al* 2022 *Nanotechnology* **33** 252001

View the [article online](#) for updates and enhancements.

### You may also like

- [Preparation and Gas Sensing Properties of SnO<sub>2</sub> Hollow Nanostructures](#)  
Junhai Wang, Xiutao Ge and Yuping Chen
- [Review—Recent Material Advances and Their Mechanistic Approaches for Room Temperature Chemiresistive Gas Sensors](#)  
Bapathi Kumar Swamy Reddy and Pramod H. Borse
- [Two-dimensional MoSe<sub>2</sub> nanosheets via liquid-phase exfoliation for high-performance room temperature NO<sub>2</sub> gas sensors](#)  
Xi Chen, Xinwei Chen, Yutong Han et al.



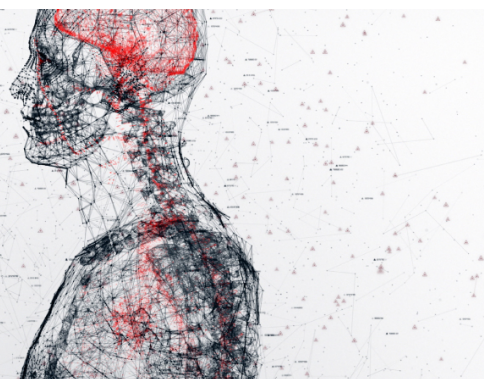
physicsworld

AI in medical physics week

20–24 June 2022

Join live presentations from leading experts  
in the field of AI in medical physics.

[physicsworld.com/medical-physics](https://physicsworld.com/medical-physics)



## Topical Review

# Gas sensing devices based on two-dimensional materials: a review

**Boran Wang, Yi Gu, Lin Chen** , **Li Ji, Hao Zhu**  and **Qingqing Sun**

State Key Laboratory of ASIC and System, School of Microelectronics, Fudan University, Shanghai 200433, People's Republic of China

E-mail: [hao\\_zhu@fudan.edu.cn](mailto:hao_zhu@fudan.edu.cn)

Received 13 December 2021, revised 27 February 2022

Accepted for publication 15 March 2022

Published 1 April 2022

**Abstract**

Gas sensors have been widely utilized penetrating every aspect of our daily lives, such as medical industry, environmental safety testing, and the food industry. In recent years, two-dimensional (2D) materials have shown promising potential and prominent advantages in gas sensing technology, due to their unique physical and chemical properties. In addition, the ultra-high surface-to-volume ratio and surface activity of the 2D materials with atomic-level thickness enables enhanced absorption and sensitivity. Till now, different gas sensing techniques have been developed to further boost the performance of 2D materials-based gas sensors, such as various surface functionalization and Van der Waals heterojunction formation. In this article, a comprehensive review of advanced gas sensing devices is provided based on 2D materials, focusing on two sensing principles of charge-exchange and surface oxygen ion adsorption. Six types of typical gas sensor devices based on 2D materials are introduced with discussion of latest research progress and future perspectives.

**Keywords:** gas sensor, two-dimensional materials, sensing, selectivity, sensitivity

(Some figures may appear in colour only in the online journal)

**1. Introduction**

With the rapid progress of industrial development generating more waste and harmful gas, more attention and great efforts have been made in precise gas detection and discrimination [1–3]. In addition to the environmental monitoring, gas sensors are also attractive in the fields of biomedicine, and are used to detect the composition and concentration of exhaled gas to diagnose diseases [4]. Food industry and even national safety also urged great demands for high-performance gas sensing technology [5].

As compared to conventional organic or electrochemical gas sensors, solid-state semiconductor gas sensor devices show advantages in high-density and CMOS-compatible integration process, and are more attractive in future system-on-chip (SoC) applications. Conventional semiconductor gas sensing technology employing semiconducting thin films like ZnO, Cu<sub>2</sub>O, In<sub>2</sub>O<sub>3</sub>, TiO<sub>2</sub> and SnO<sub>2</sub> have been widely

investigated and commercially implemented in practical applications [6–11]. However, the metal oxide-based gas sensor requires a relatively strict environment during operation, and a higher operating temperature is usually necessary to increase the chemical reaction activity with the gas, which will inevitably increase energy consumption and baseline drift, making it difficult to be used in daily environments. On the other hand, although conductive polymers can be used as sensing materials for gas sensing at room temperature, their performance will be greatly affected by humidity.

Nowadays, with the development of advanced ultra-thin low-dimensional semiconductors and devices, two-dimensional (2D) materials-based gas sensing technology has drawn great attention in building high-density, low-power and high-sensitivity gas sensor devices. Due to the intrinsic nature of atomic-level thickness of 2D materials, the constructed gas sensors utilizing the high surface-to-volume feature of the materials are expected with high sensitivity and recovering

efficiency [12]. In addition to the large surface-to-volume ratio, 2D materials have good semiconducting or conducting properties, which make them promising in gas sensing device applications. 2D materials can not only be modified on the surface, but also can be modified between layers due to the relatively weak van der Waals interlayer force, which distinguishes 2D materials from other materials systems like zero-dimensional (0D) and one-dimensional (1D) analogues. In comparison, although 0D and 1D materials also shows advantages in high surface-to-volume ratio, they face difficulties in device integration with robust electrical contacts. Besides, the layered structure of 2D materials also enables fabrication of various heterojunction gas sensing devices, providing more ways and possibilities for improving gas sensing performance.

In general, 2D materials can be divided into various categories: (1) graphene-family [13–16]; (2) transition metal dichalcogenides (TMDCs) like MoS<sub>2</sub> [17, 18], WS<sub>2</sub> [19, 20], WSe<sub>2</sub> [21, 22], and so forth [23, 24]; (3) MXenes including transition metal carbide/carbon oxides [25]; (4) single-element layered materials, such as black phosphorus [26, 27], arsenene [28], and antimonene [29, 30]; (5) 2D metal oxides. Such semiconducting or conducting 2D materials effectively enables the field-effect transistor (FET)-type gas sensors or resistor-type gas sensors, and have broad prospects in the application of low-power, high-sensitivity gas sensors applications.

In this review, we first introduce the sensor and gas reaction mechanisms based on different materials. Then, various types of gas sensors are discussed and reviewed with current research status of gas sensing based on different 2D materials and heterojunctions. In addition, the application of 2D materials in future advanced gas sensors are prospected.

## 2. Gas sensing mechanisms

### 2.1. Surface adsorbed oxygen ions mechanism

The surface adsorption of oxygen ions is the main mechanism for traditional metal oxide-based gas sensors. Part of the electrons can be transferred from the top of the valence band to the bottom of the conduction band in the metal oxide at high temperatures. Environmental O<sub>2</sub> in the surroundings can be physically or chemically adsorbed on the surface of the metal oxide [11]. Electrons near the surface of metal oxides can be captured by O<sub>2</sub> in the conduction band and become negatively charged oxygen anions, including O<sup>2-</sup>, O<sup>-</sup> and O<sub>2</sub><sup>-</sup>, the type of which is dependent on the surface temperature. Oxygen anions will interact with the measured gas, thereby changing the conductivity of the metal oxide.

Different species of oxygen ion will appear on the surface of the gas sensor at different temperatures. For example, at operating temperatures of 300 °C–450 °C [31], O<sup>-</sup> is considered to be dominant. This is the operating temperature of most metal oxide gas sensors. The reaction formula of

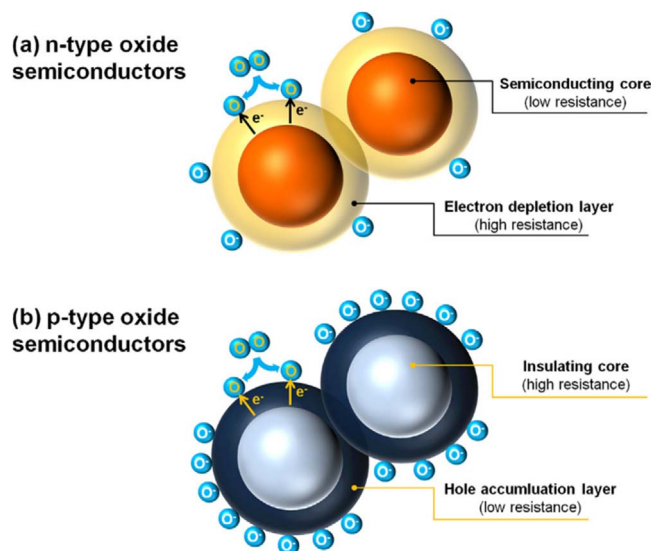
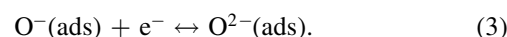
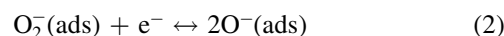
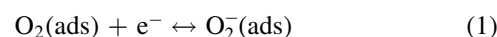


**Figure 1.** Schematic diagram of the formation of electron core-shell structures in n-type and (b) p-type oxide semiconductors. Reprinted from [33], Copyright © 2013 Elsevier B.V. All rights reserved.

different temperatures is shown in the following formula [32]:



Metal oxides can be divided into p-type and n-type, as shown in figure 1. For metal oxide gas sensors, most of the charge carriers in the n-type and p-type sensors are electrons and holes, respectively. When the affinity energy of the gas molecules exceeds the work function of the metal oxide semiconductor surface, electrons are transported from the semiconductor surface to the gas molecules, resulting in negative ion adsorption of the gas. On the contrary, when the affinity energy of gas molecules is lower, the gas will lose electrons and form positive ion adsorption.

For n-type sensing materials (including ZnO, TiO<sub>2</sub>, SnO<sub>2</sub>, etc), the resistance will decrease when exposed to reducing gases. Conversely, resistance increases when exposed to oxidizing gas. The sensing results are opposite for p-type sensing materials (including CuO, NiO, etc). Furthermore, the metal oxide gas sensor can also be realized in a p-n junction structure, like CuO(p)/ZnO(n) [34–36] and NiO/SnO<sub>2</sub> [37–39], which have shown enhanced gas sensing response due to enlarged surface depletion regions and increased potential barriers. Meng *et al* has built a gas sensor based on NiO/SnO<sub>2</sub> [40]. When SnO<sub>2</sub> (n-type) and NiO (p-type) are in close contact, electrons will move from SnO<sub>2</sub> to NiO. In addition, the holes will move in the opposite direction from NiO to SnO<sub>2</sub> until the system reaches the Fermi level equilibrium, resulting in the formation of a self-built electric field in the interface area [40]. At the heterojunction interface, a broad electron depletion layer is generated, and a potential barrier is formed at the curvature of the p-n heterojunction. The depletion layer will expand radially from the NiO nanoparticles due to the formation of a significant number of p-n heterojunctions at the interface. According to

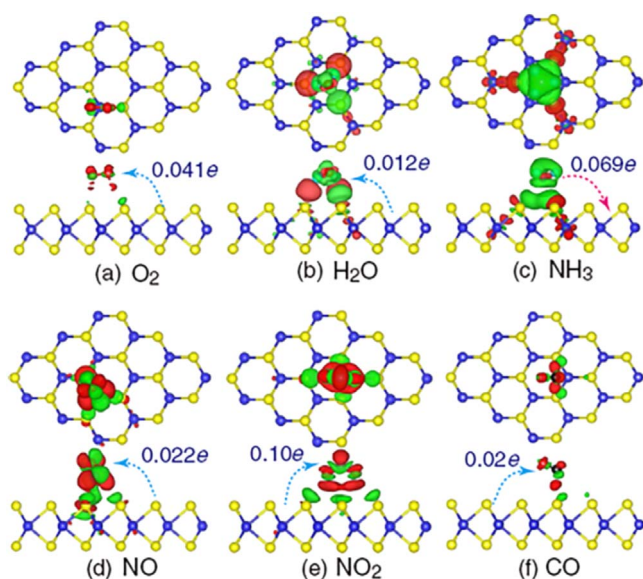


**Figure 2.** Charge transfer process and density difference plots for (a)  $O_2$ , (b)  $H_2O$ , (c)  $NH_3$ , (d)  $NO$ , (e)  $NO_2$ , and (f)  $CO$  interacting with monolayer  $MoS_2$ . Reproduced from [41]. CC BY 2.0.

semiconductor theory, the height of the barrier affects resistance and thus realizing gas sensing. Therefore, this method of expanding the surface depletion region greatly reduces the conductive area and increases the barrier height to improve gas sensing.

## 2.2. Charge-transfer mechanism

For 2D materials, gas sensing mainly follows the charge-transfer processes mechanism. The sensing material is the acceptor or donor of charge during the charge transfer procedure. When the 2D material-based gas sensor is exposed to gas, a charge transfer occurs between the 2D material and the gas. Because when different gases react with the same material, the direction of charge transfer and the amount of charge transferred are different, resulting in different changes in the sensor, and therefore, gas identification and classification is achieved.

For n-type 2D materials like  $MoS_2$ , figure 2 shows a schematic diagram of the charge transfer that occurs when monolayer  $MoS_2$  is exposed to  $NO$ ,  $O_2$ ,  $NH_3$ ,  $H_2O$ ,  $NO_2$ , and  $CO$  [41]. When the n-type  $MoS_2$  film is exposed to  $NO$ ,  $O_2$ ,  $H_2O$ ,  $NO_2$  and  $CO$  gas, the electron charge is transferred from the film to the gas, causing a decrease in the electron concentration in the  $MoS_2$  film and an increase in resistance. When the n-type  $MoS_2$  film is exposed to  $NH_3$ , electron charges are transferred from the gas to the film. This will increase the electron concentration on the  $MoS_2$  film, and the resistance decreases.

For p-type 2D materials like typical  $WSe_2$ , figure 3 shows that the surface of  $WSe_2$  has the charge consumption of  $H_2O$ ,  $CO$ ,  $NO$ ,  $O_2$  and  $NO_2$  adsorbents, while figure 3(f) shows that a charge accumulation area is generated near the  $WSe_2$  monolayer adsorbing  $NH_3$  [42].

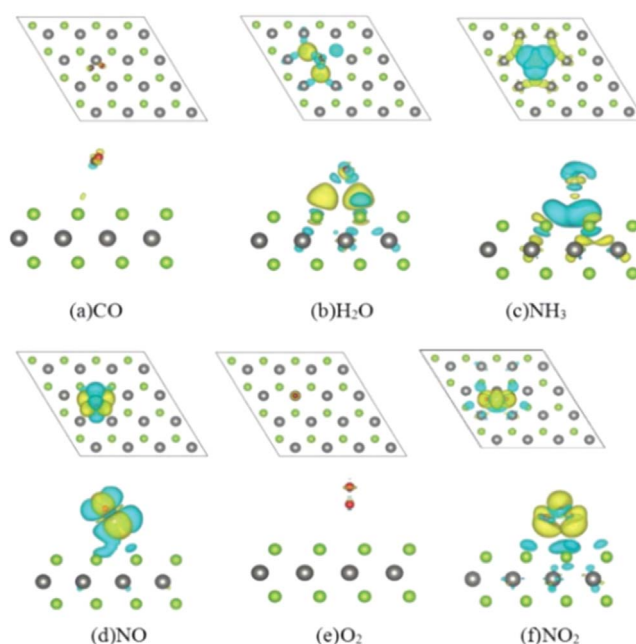


**Figure 3.** An iso-surface map of the difference in electronic charge density of (a)  $CO$ , (b)  $H_2O$ , (c)  $NH_3$ , (d)  $NO$ , (e)  $O_2$ , and (f)  $NO_2$  on a  $WSe_2$  monolayer. Yellow and blue colors are used to indicate charge accumulation and consumption, respectively. Reproduced from [42] with permission from the Royal Society of Chemistry.

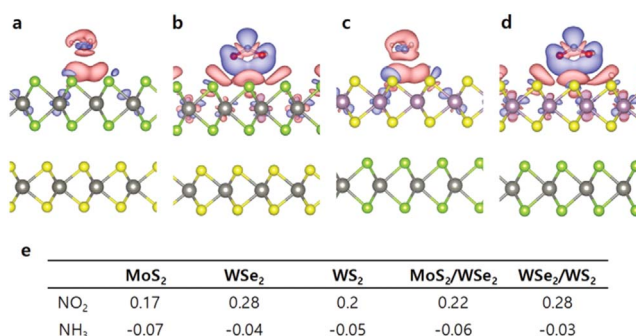


**Figure 4.** The difference in charge density of (a)  $NH_3$ , (b)  $NO_2$  adsorbed on the  $WSe_2/WS_2$  heterostructure and (c)  $NH_3$ , (d)  $NO_2$  adsorbed on the  $MoS_2/WSe_2$  heterostructure was obtained by DFT calculations. (e) The calculation result of the transfer charge between the gas molecule and the 2D materials. [43] John Wiley & Sons. © 2020 Wiley-VCH GmbH.

From the above studies, for the same gas, the amount of charge transferred between different 2D materials and gases is also different, which reflects the selectivity of gas sensing materials. Figure 4 is an equivalent diagram of the charge exchange of three different materials to different gases.  $MoS_2$  and  $WS_2$  are generally n-type materials, and  $WSe_2$  generally belong to p-type material family [43]. From figure 4(e), it is concluded that the reaction of different materials to reducing gas ammonia and oxidizing gas  $NO_2$  is quite different. Due to the fact that the majority carriers of n-type and p-type 2D materials are electrons and holes, respectively, the same gas typically has the opposite effect on the resistance on n-type and p-type 2D materials.



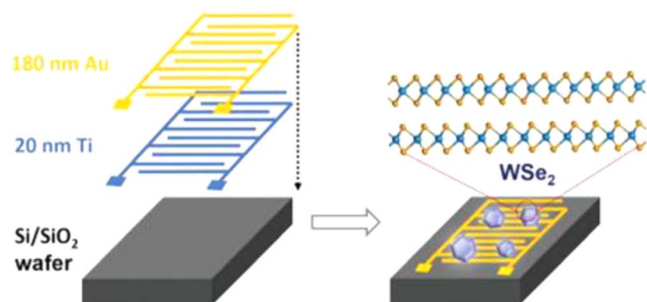


**Figure 5.** The resistor-type gas sensor built on WSe<sub>2</sub> with Au/Ti as the interdigital electrode. Reproduced from [44] with permission from the Royal Society of Chemistry.

At present, gas sensors are mainly based on two mechanisms: surface adsorbed oxygen ions mechanism and charge-transfer mechanism. Various gas sensors have been derived on the basis of these two mechanisms which will be introduced in the following sections.

### 3. The various types of gas sensors

#### 3.1. Resistor-type gas sensors

Resistor-type gas sensors have been used in the preparation of gas sensing devices with different sensing materials, such as 2D materials, metal oxides, metal-organic framework (MOF), and so on.

The working mechanism of the resistor type gas sensor is that: when the target gas contacts the sensing material, the gas changes the resistance of the material through a molecular exchange mechanism or an oxygen ion adsorption mechanism. Therefore, the method of testing factors such as the amount of change in the resistance of the material and the resistance change time can be used to monitor the concentration of a certain gas and accurately identify the gas.

The advantages of chemical resistors include simple manufacturing, relatively low cost, convenient use, and so on. Chemical resistors mainly include a wafer, interdigital electrodes (or two metal electrodes), and sensing materials used to sense gas. Figure 5 is an interdigital electrode resistor-type gas sensor based on the 2D WSe<sub>2</sub> [44].

Acharyya *et al* have demonstrated a gas sensor based on SnO<sub>2</sub> hollow spheres, as shown in figure 6. The sensor is used to identify different volatile organic chemical (VOC) gases, including 2-propanol, formaldehyde, methanol and toluene. They followed the Eley-Rideal model and performed a kinetic analysis of the conductance transient of SnO<sub>2</sub> gas sensor. Finally, the visualization of VOC discrimination and recognition is realized [45].

Merry *et al* demonstrated a chemical resistance gas sensor based on a conductive MOF. The sensor substrate is a shrinkable polymer film with miniature graphite electrodes, which is shown in figure 7(a). The gas sensor can distinguish NH<sub>3</sub>, H<sub>2</sub>S, and NO at the ppm level, as shown in figure 7(b). In addition, principal component analysis (PCA) confirmed that the sensor can distinguish H<sub>2</sub>S and NO at different

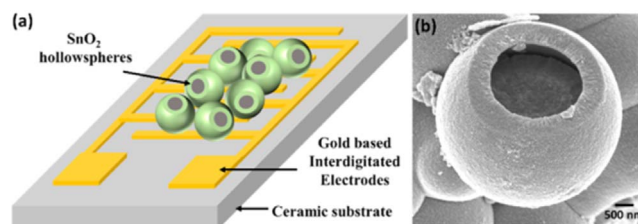


**Figure 6.** (a) Schematic diagram of the gas sensor based on SnO<sub>2</sub> hollow spheres. (b) SEM image of the sensing material. Reprinted with permission from [45]. Copyright © 2021, American Chemical Society.

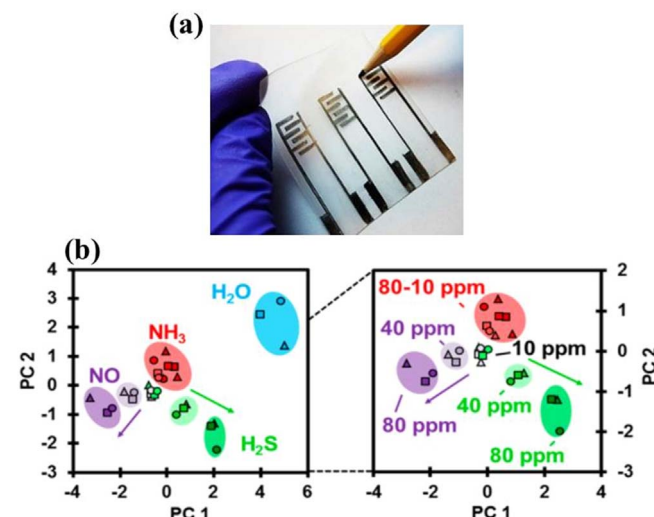


**Figure 7.** (a) Shrinkable polymer film with graphite interdigital electrodes. (b) Schematic diagram of principal component analysis of sensor arrays. Reprinted with permission from [46]. Copyright © 2016, American Chemical Society.

concentrations, and can distinguish 80 ppm from 40 and 10 ppm [46]. The sensing response of a chemiresistors is generally defined as follows:

$$S(\%) = [(R_g - R_{air})/R_{air}] \times 100\%$$

in which  $S$  represents the response rate, that is, the ratio of the resistance difference between the gas sensor and the target gas after the reaction to the resistance before the reaction.  $R_{air}$  is the initial resistance of the sensor in the air, and  $R_g$  is the resistance after the resistive gas sensor exposes to the target gas.

#### 3.2. Non-resistor-type gas sensors

**3.2.1. Field-effect transistor.** Field-effect transistor (FET) type gas sensor is a commonly used sensor structure, which has high sensitivity for detecting the target gas, with simple manufacturing process and convenient portability. At present, the FET-type gas sensor has been miniaturized to the nanometer level. The sensing material can be used as a gate or channel of the FET. The threshold voltage or drain current

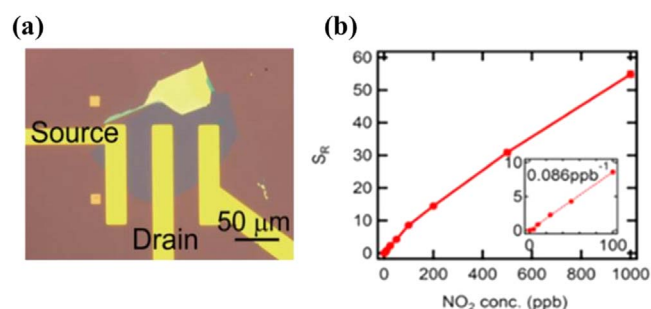


**Figure 8.** (a) Schematic diagram of the device under the microscope (b) resistance-based sensor response varies with NO<sub>2</sub> gas concentration. Reprinted with permission from [49]. Copyright © 2021, American Chemical Society.

of these sensors will change upon exposure to the target gas, which provides electrical signals for further data processing.

The difference between the gas response characteristics of the resistance-type and FET-type gas sensors manufactured has been experimentally verified by Jung *et al.* In an atmosphere of 105 °C 500 ppb NO<sub>2</sub> gas, the FET-type gas sensor shows a better response, which is about 8.15 times higher than that of the resistance-type gas sensor. The advantages of the FET-type gas sensor are not only the small size and low noise, but also the high sensitivity and response, making it more prevalent in current semiconductor gas sensing techniques [47].

Shin *et al* also demonstrated experimental work comparing the resistance-type and FET-type gas sensors fabricated on the same wafer [48]. An n-type In<sub>2</sub>O<sub>3</sub> thin film prepared by radio frequency magnetron sputtering serves as the sensing material. The resistance-type gas sensor uses interdigital electrodes, and the sensitive material is made above the electrodes. A FET device is also fabricated with a floating gate and a control gate. It has been found that as compared with resistive gas sensors, FET-type gas sensors have a constant gas-to-air noise ratio during the gas reaction process [48]. Tabata *et al* showed a gas sensor based on MoS<sub>2</sub> FET structure, which is shown in figure 8(a). Resistance-based sensor response increases in response to increasing NO<sub>2</sub> concentration. From the slope of the curve of 100 ppb, the accuracy of the sensor can be obtained as 8.6%/ppb, as shown in figure 8(b). They also explored the photoactivation response of the gas sensor to NO<sub>2</sub> gas under visible light, and studied the detection mechanism of the MoS<sub>2</sub> gas sensor [49].

Hazra *et al* fabricated a back-gate graphene oxide FET-type gas sensor device based on a p-Si substrate with 90 nm SiO<sub>2</sub> [50]. They confirmed that the sensor has different responses for the same gas under different  $V_{GS}$ . In a methanol atmosphere of 150 ppm at 100 °C, the sensitivity of the sensor is 1.95% at  $V_{GS} = 0$  V. When  $V_{GS}$  is 5 V and 13 V, the response of the sensor is 127.93% and 82.38%, respectively [50].

**3.2.2. Schottky junction.** The difference in work function between metals and semiconductors enables metal–semiconductor heterostructure, which has typical types of rectifying Schottky junction and non-rectifying Ohmic

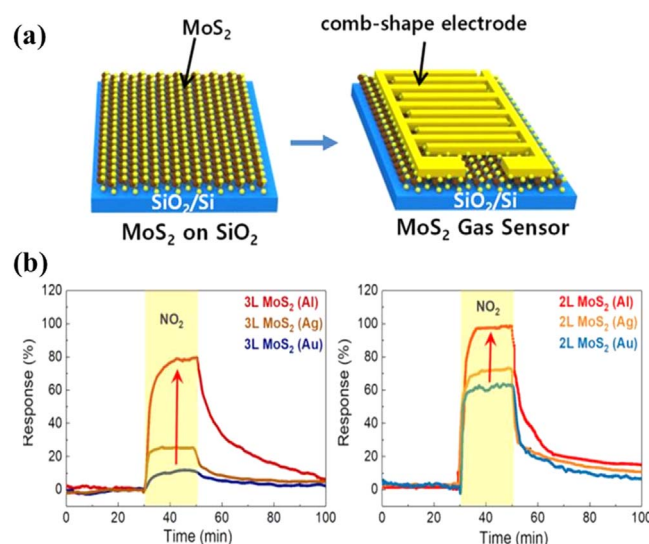


**Figure 9.** (a) The schematic diagram of the MoS<sub>2</sub> device. (b) The response to 10 ppm NO<sub>2</sub> for 2L and 3L MoS<sub>2</sub> with Al, Ag, and Au electrodes. Reprinted with permission from [52]. Copyright © 2019, American Chemical Society.

contact. Ricciardella *et al* obtained the Schottky junction based on the solution-processed multilayer graphene (MLG) method [51]. When graphene is in contact with silicon, a space charge zone is formed. With the accumulation of positive and negative charges, it eventually reaches an equilibrium state forming a Schottky junction.

Kim *et al* demonstrated a gas sensor based on MoS<sub>2</sub>-Au Schottky contact. The schematic diagram of the device is shown in figure 9(a). They control the SBH by changing the metal type of the device electrode to improve the response of the gas equipment to different gases. The layer number of MoS<sub>2</sub> and the types of metal electrode will affect the gas response, which is shown in figure 9(b). With a constant MoS<sub>2</sub> layer number, the lower the metal work function of the device, the higher the response to NO<sub>2</sub> [52].

Mahmoodnia *et al* demonstrated a GaAs-based Schottky junction gas sensor, and saturated ammonium sulfide solution was used to passivate the GaAs [53]. The barrier height of the GaAs gas sensor after passivation has changed from 0.688 eV to 0.758 eV. At 150 °C, the responsivity of the passivated GaAs gas sensor to 600 ppm ammonia gas increased significantly from 26% to 63%. In addition, its response time and recovery time are also greatly reduced [53].

After the sensing material adsorbs the target gas molecule, the Fermi level of the semiconductor heterojunction and the Schottky barrier height of the interface can be adjusted. The Schottky barrier height is influenced by the density of adsorbed gas molecules and the reverse current through the device changes with the Schottky barrier height. Therefore, the Schottky junction gas sensor has the characteristics of high sensitivity and easy manufacturing [54, 55].

**3.2.3. Heterojunction.** Semiconductor p-n heterojunctions are formed with p-type and n-type semiconductor materials

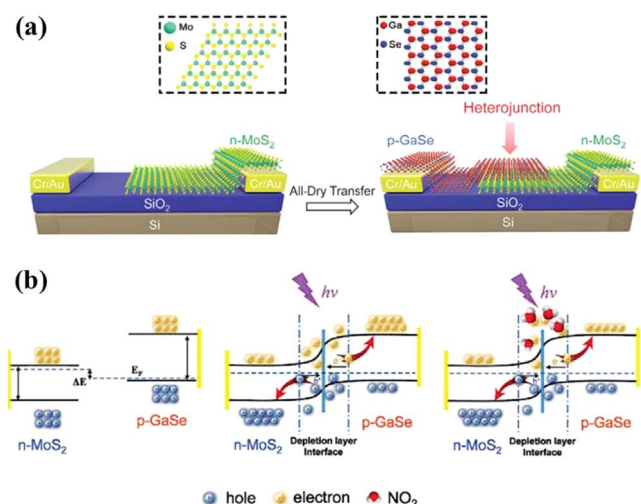


**Figure 10.** (a) The structure diagram of the MoS<sub>2</sub>/GaSe heterojunction gas sensor. (b) Sensing mechanism of heterojunction gas sensor. The left is the energy band diagram of MoS<sub>2</sub> and GaSe, the middle is the energy band diagram of the heterojunction of the two materials under light, and the right is the energy band diagram of the heterojunction exposed to NO<sub>2</sub>. Reproduced from [56]. CC BY 4.0.

which can overcome the shortcomings of single-material gas sensors through the formation of heterostructure interfaces. Figure 10(a) shows a MoS<sub>2</sub>/GaSe heterojunction gas sensor [56]. A built-in electric field is generated within the heterojunction due to the difference in Fermi level, which causes the conduction band and valence band of the interface to bend. The band change of the heterojunction gas sensor before and after sensing is shown in figure 10(b). Holes and electrons flow in opposite directions, and they will gradually reach equilibrium forming a thick space charge region.

Dhara *et al* showed a gas sensor based on WSe<sub>2</sub>/MoS<sub>2</sub> heterojunction, as shown in the figures 11(a) and (b). They compared the effect of MoS<sub>2</sub> thickness on response performance in WSe<sub>2</sub>/MoS<sub>2</sub> heterojunction. Obviously, the thinner MoS<sub>2</sub> sheet has a higher response current change, as shown in the figures 11(c) and (d). Through the detection of NO<sub>2</sub> and TNT, it is proved that the diode has a wide range of applicability, and the response to TNT is three times stronger than that of FET [57].

According to the oxidation or reduction properties of the measured gas, electrons are released or retracted between the gas molecules and the p-n junction device. The width of the space charge or depletion layer varies with the charge carriers of the p-n heterojunction. The sensing performance of a heterojunction is related to the area coverage and interface bonding of two different materials. Because the electrons passing through the material are directly proportional to the material coverage, the charge transfer between the material with higher area coverage and gas molecules is stronger than the material with lower area coverage [58]. Heterojunction gas sensors can not only enhance the gas-sensing effect, but also provide alternative approaches to solve the problem of poor sensing selectivity of the single material-based sensor devices.

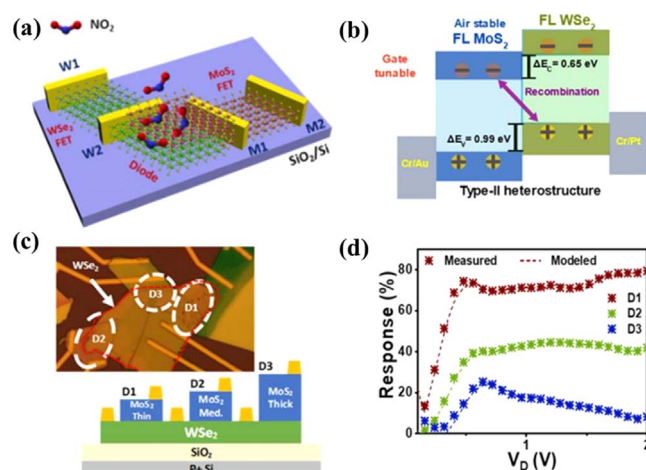


**Figure 11.** (a) Structure of WSe<sub>2</sub>/MoS<sub>2</sub> heterojunction. (b) Energy band diagram of WSe<sub>2</sub>/MoS<sub>2</sub> pn diode. (c) Schematic diagram of the same substrate with different thicknesses of MoS<sub>2</sub>. (d) Response comparison of different MoS<sub>2</sub> thicknesses. Reprinted with permission from [57]. Copyright © 2021, American Chemical Society.

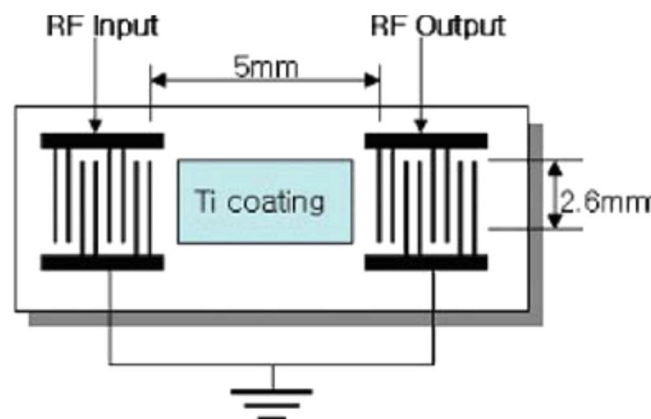


**Figure 12.** Schematic diagram of SAW gas sensor configuration. Reproduced from [59], with permission from Springer Nature. Copyright © 2006, Springer Science Business Media, LLC.

**3.2.4. Surface acoustic waves (SAW) gas sensor.** Research on SAW equipment used in gas sensors has been experimentally studied. In SAW gas sensors, various factors such as mass load, elastic load, electrical load, and acoustic-electric coupling will affect the sensing responsivity. The detection principle of SAW gas sensor depends on the mass load effect of gas absorption to change the SAW propagation characteristics. Yoo *et al* demonstrated a SAW sensor that can measure volatile gases such as methanol, acetone, and ethanol. The SAW sensor is mainly composed of input and output interdigital transducer and quality sensitive layer, as shown in figure 12 [59].

The sensitivity of SAW gas sensors is relatively high because most of the wave energy is concentrated in one or two wavelengths near the crystal surface. In its first-order approximation of surface waves, it is highly sensitive to any changes including physical or chemical properties of the thin active layer placed on the crystal surface [60].



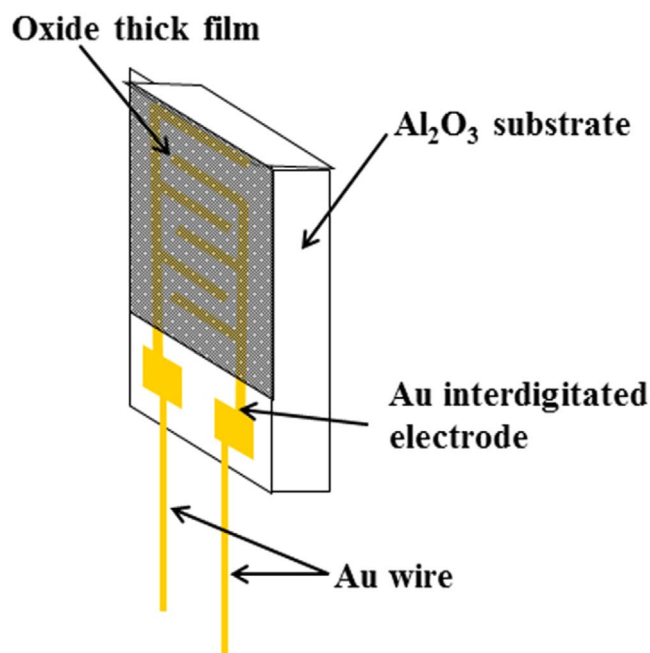


**Figure 13.** Schematic diagram of impedance metric carbon monoxide sensor. Reprinted from [64], © 2017 Elsevier B.V. All rights reserved.

Luo *et al* demonstrated a SAW type gas sensor. The sensing layer for NO<sub>2</sub> gas detection is Bi<sub>2</sub>S<sub>3</sub> nanobelt, which is coated on the SAW device [61]. At room temperature, the gas sensor has a response of 2 kHz under 10 ppm NO<sub>2</sub>. According to theoretical calculations, the detection limit of the gas sensor is 17 ppb.

Til now, SAW gas sensors have received widespread attention because of their good stability, high sensitivity, small size, wireless sensing in inaccessible areas and other characteristics.

**3.2.5. Impedance-type gas sensor.** Impedance sensor is a mixed potential sensor based on impedance change. It calculates the impedance in the frequency domain by applying a sinusoidal voltage and measuring the current. The change in the complex impedance reflects the change in the concentration of a specific gas species in a quantitative manner [62]. At present, impedance gas sensors have been used to detect various gases such as NO [63], CO [64], NOx [65], and H<sub>2</sub>O [66].

The structure of an impedance gas sensor based on an La<sub>1.9</sub>Ce<sub>0.1</sub>CuO<sub>4</sub> oxide film is shown in figure 13. The thick-film device responded well to CO between 50 and 600 ppm at 400 °C–500 °C and 50 Hz [64].

Compared with traditional sensors, impedance sensors have specific advantages like accurate detection of single ppm gaseous substances under high background O<sub>2</sub> concentration [65]. However, the accompanying electronic equipment and signal processing equipment are more complicated and relatively difficult to implement [62].

For a short conclusion, resistor-type and non-resistor-type (which further includes types of FET, Schottky junction, heterojunction, and so forth), gas sensors have been

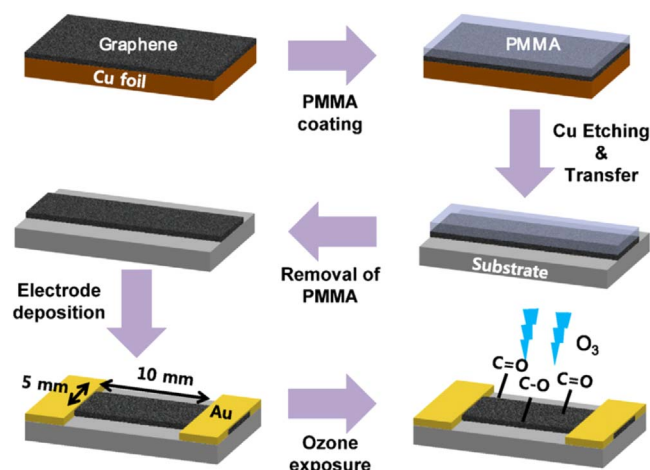


**Figure 14.** Flow chart of the fabrication process of an ozone-treated graphene-based gas sensor. Reprinted from [69], Copyright © 2012 Elsevier B.V. All rights reserved.

introduced with representative works. Advantages and disadvantages of each type are comparatively analysed, which suggests that materials, device structures should be carefully engineered towards different sensing gases in practical applications.

## 4. Gas sensing with 2D materials

### 4.1. Graphene

2D graphene has been extensively studied in gas sensing applications. In 2007, Schedin *et al* reported that graphene can be used for gas molecule detection, confirming that the charge carrier density of graphene changes with the adsorption or desorption of surface gas molecules [67]. Since then, research on graphene gas sensors has attracted great attention. Hwang *et al* prepared graphene with high crystal quality by using mechanical cracking of highly oriented pyrolytic graphite (HOPG) [68]. The graphene can be used to detect and identify NH<sub>3</sub> and NO<sub>2</sub>, and experiments have verified that the response to NH<sub>3</sub> is mainly determined by the L/W ratio rather than the number of graphene layers.

Large regions of high-quality intrinsic graphene can be fabricated using chemical vapor deposition (CVD). Chung *et al* used ozone to treat graphene by CVD for the purpose of improving the graphene sensing performance (figure 14). The optimal density of oxygen functional groups can be easily introduced into the graphene surface by regulating the ozone treatment period. They showed that the sensor has a high responsivity to NO<sub>2</sub> gas with low concentration of ppb level. The response speed is eight times faster than the original graphene sensor [69].

Graphene-based gas sensors can also be based on different substrates. Choi *et al* realized a large-scale transparent graphene gas sensor on a flexible substrate [70]. In a 0.5 ppm NO<sub>2</sub> gas atmosphere, the response rate is 10%, as shown in figure 15(b). At a bending strain rate of 1.4%, the gas sensitivity ratio  $\Delta R/R_0$  for 1 ppm NO<sub>2</sub> gas is 12%, as shown in



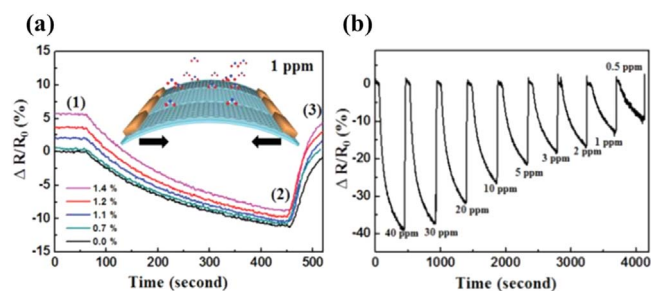


**Figure 15.** (a) The response rate when heated at 100 °C–165 °C under NO<sub>2</sub> (1 ppm) with a bending strain of 0%–1.4%. (b) The resistance responds to 40–0.5 ppm NO<sub>2</sub> gas. [70] John Wiley & Sons. © 2014 WILEY-VCH Verlag GmbH & Co. KGaA, Weinheim.

figure 15(a). The graphene in this experiment was synthesized by CVD.

Graphene decoration is further studied to achieve more sensing gas types with improved performance. For example, bare graphene does not respond to hydrogen [71], and Chu *et al* used epitaxial graphene deposited on a SiC substrate by a CVD method and coated with platinum for hydrogen detection [72]. The gas sensor can be used to detect 1% of H<sub>2</sub>. Johnson *et al* demonstrated the fabrication and application of Pd functionalized multilayer graphene nanoribbons network for hydrogen sensing through experiments. It achieves a response rate of approximately 55% to 40 ppm H<sub>2</sub> at room temperature [73].

Ovsianytzkyia *et al* reported a graphene-based high-sensitivity H<sub>2</sub>S gas sensor decorated with silver nanoparticles (AgNPs) and charged impurities. The device shows capability of repeatable detection of H<sub>2</sub>S gas within six minutes, with high selectivity and a detection limit of less than 100 ppb [74].

In addition to metals, metal oxides, sulfides, polymers and other doping methods are also utilized to improve the gas sensitivity of graphene. The ZnO/graphene composite material can provide a gas response of up to 513 in an atmosphere of 1000 ppm ethanol. The gas response of the composite material is nearly 5.0 times higher than that of pure ZnO [75].

Wu *et al* used MOF-on-SLG (MOF: metal-organic framework, SLG: single-layer graphene) structure synthesized by epitaxial growth of MOFs on SLG to identify NH<sub>3</sub>, O<sub>2</sub>, and CO. The device structure is shown in figure 16(a). By fitting the model, the relevant parameters are extracted from figure 13(c). Based on the characteristic  $k$  value and the unique electronic response  $r_0$ , the recognition function of different gases (NH<sub>3</sub>, O<sub>2</sub>, CO,) can be realized, as shown in figure 16(b) [76].

Jang *et al* decorate graphene with synthetic Ag<sub>2</sub>S nanoparticles to enhance gas selectivity and improve the response of graphene-based chemical sensors. When the gas sensor was exposed to acetone vapor, it showed a response that was 660% higher than the pristine graphene [77]. Eom *et al* introduced non-noble metals as sensitizers on hybrid metal oxide/graphene fibers to improve the performance of chemical resistance sensors. At 150 °C, the sensitivity of Ni/

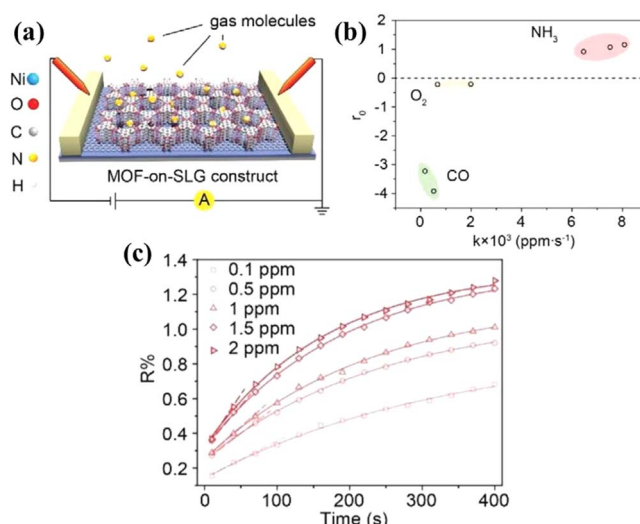


**Figure 16.** (a) Schematic diagram of the device composed of Ni-CAT-1-on-SLG structure. (b) Schematic diagram of gas recognition based on characteristic  $k$  value and unique electronic response  $r_0$ . (c) The response to different concentrations of NH<sub>3</sub> and the fitting of the first-order kinetic model. Reproduced from [76]. CC BY 4.0.

NiO/grapheme and Cu/Cu<sub>2</sub>O/graphene fiber sensors to 5 ppm NO<sub>2</sub> gas is 18.90% and 0.82%, respectively [78].

#### 4.2. Transition metal dichalcogenide

Transition metal dichalcogenides (TMDs) are a class of materials with the molecular formula MX<sub>2</sub> with M representing transition metal elements, including Mo, W, Ti, Zr, Re, etc and X representing chalcogen element, including Se, S, or Te [79]. For example, typical MoS<sub>2</sub> has a large surface area to volume ratio and excellent semiconductor characteristics, the atomic thin-layer MoS<sub>2</sub> has great potential in gas sensing applications. Liu *et al* used Schottky contact-based single-layer MoS<sub>2</sub> as a high-performance room temperature chemical sensor for the first time [80]. This MoS<sub>2</sub> sensor can clearly detect NO<sub>2</sub> and NH<sub>3</sub> with concentrations as low as 20 ppb and 1 ppm, respectively. Kumar *et al* proved that multi-layer MoS<sub>2</sub> grown by CVD under ultraviolet irradiation at room temperature can achieve ultra-fast detection of NO<sub>2</sub> gas and excellent recovery [81]. Under ultraviolet radiation and at room temperature, the gas sensor shows rapid recovery, with a low response time of 29 s and a high response of 35.16%.

Besides CVD method, the MoS<sub>2</sub> flakes obtained by mechanical exfoliation are also used for gas sensing study. Li *et al* used scotch tape to obtain single-layer and multi-layer MoS<sub>2</sub> films on Si/SiO<sub>2</sub> substrates by mechanical exfoliation technique, and fabricated n-type FETs (figure 17) [82], which are further used for NO detection. But it was found that the single-layer MoS<sub>2</sub> FET detection results were not stable. The 2L, 3L, and 4L MoS<sub>2</sub> FETs show good sensitivity and stability, even responding to 0.8 ppm NO.

Similar to graphene, decorating functional metal to the surface of the MoS<sub>2</sub> film can also optimize gas sensing performance. Baek *et al* [83] fabricated a Pd-functionalized MoS<sub>2</sub> sensor, which has a high sensitivity to hydrogen, which

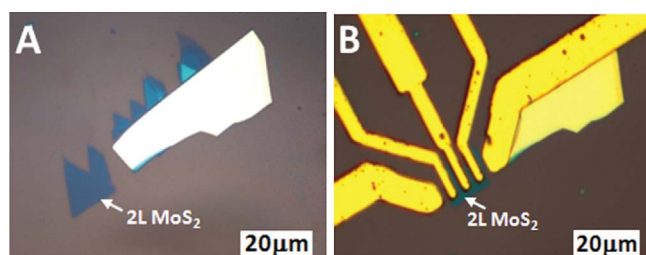


**Figure 17.** Optical microscope image of (a) 2L MoS<sub>2</sub> on Si/SiO<sub>2</sub> substrate. (b) A back-gate FET device based on 2L MoS<sub>2</sub> film, where Au electrodes are used as source and drain electrodes. [82] John Wiley & Sons. Copyright © 2012 WILEY-VCH Verlag GmbH & Co. KGaA, Weinheim.

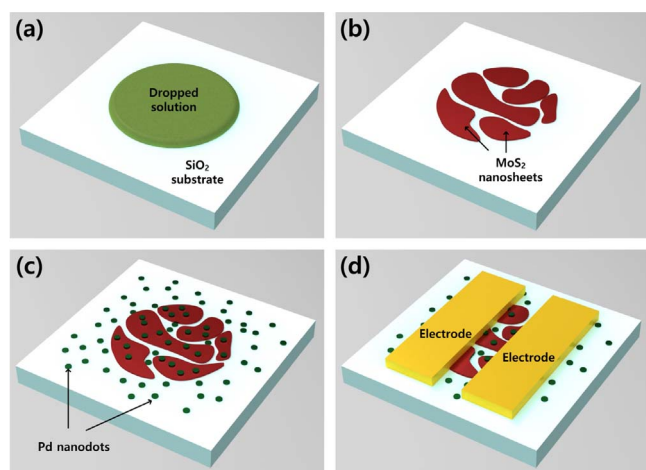


**Figure 18.** Fabrication process of sensors based on Pd-MoS<sub>2</sub>. Reprinted from [83], © 2017 Elsevier B.V. All rights reserved.

is shown in figure 18. The thickness of Pd has shown a great impact on gas sensing. When the 5 nm Pd functionalized MoS<sub>2</sub> sensor is exposed to 1% hydrogen, the gas response is −35.3%, and the response time is 13.1 min. In order to adjust the VOC gas response and gas recognition, Cho *et al* [84] used MoS<sub>2</sub> decorated with Au nanoparticles as the channel. In contrast to the original MoS<sub>2</sub>-based gas sensor, this gas sensor has a negative response to the oxygen-functionalized VOC ethanol and acetone. The electrical response to toluene and hexane is positive, which is similar to MoS<sub>2</sub>. These methods successfully changed the single response of MoS<sub>2</sub> to different VOCs.

In addition to metal doping, MoS<sub>2</sub> can also be combined with oxides to improve gas sensing properties. He *et al* prepared an SnO<sub>2</sub>/MoS<sub>2</sub> sensor to detect SO<sub>2</sub> through hydrothermal reaction. The SnO<sub>2</sub>/MoS<sub>2</sub> sensor detects 1 ppm SO<sub>2</sub> and has a good response of 4.68 under UV light conditions [85].

WS<sub>2</sub>, another typical TMD semiconductor has also been widely implemented in gas sensing device applications. Huo *et al* mechanically exfoliated the multi-layer WS<sub>2</sub> nanoflake from the WS<sub>2</sub> crystal to a 300 nm SiO<sub>2</sub>/Si substrate and fabricated a FET device [86]. The device has a good response to reducing gases, especially NH<sub>3</sub> molecules, but it is not very sensitive to O<sub>2</sub> molecules. Under light, due to the increase of

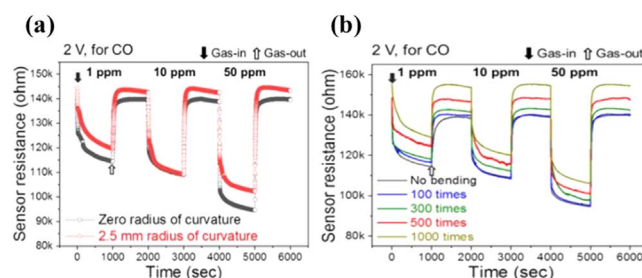


**Figure 19.** The dynamic resistance curve of the Au functionalized WS<sub>2</sub> gas sensor to 50 ppm CO under a voltage of 2 V (irradiation for 15 s). (a) Comparison of gas response without bending and with a radius of curvature of 2.5 mm. (b) Comparison of gas response without bending and with a radius of curvature of 4 mm with different bending cycles. Reprinted from [88], © 2020 Elsevier B.V. All rights reserved.

electron-hole pairs, all gas molecules can be adsorbed further, and the gas sensitivity to O<sub>2</sub> increases, but the sensitivity to ethanol and NH<sub>3</sub> decreases [86].

Kim *et al* reported a WS<sub>2</sub>-based selective CO gas sensor on a flexible substrate [87]. WS<sub>2</sub> nanosheets functionalized with Au can improve the sensitivity of the gas sensor and the selectivity of CO gas. The gas sensor can still maintain good CO sensing characteristics even after multiple mechanical folding [88], as shown in figure 19. Kuru *et al* showed a hydrogen sensor based on WS<sub>2</sub> nanosheet-Pd nanoparticle composite film. The sensor is based on a polyimide substrate and can also be bent multiple times [87].

In order to enhance the sensitivity of gas sensor, Qin *et al* decorated WS<sub>2</sub> nanosheets with TiO<sub>2</sub> quantum dots [89]. Different TiO<sub>2</sub>/WS<sub>2</sub> molar ratios will lead to different gas sensing effects. In an atmosphere of 250 ppm NH<sub>3</sub>, the response of the TiO<sub>2</sub> QDs/WS<sub>2</sub> nanohybrid with the best molar ratio is 17 times larger than that of the single-layer WS<sub>2</sub>. The gas sensor is relatively stable, and the sensitivity hardly drops after several test cycles.

Ko *et al* showed a gas sensor with high response to NO<sub>2</sub> based on WSe<sub>2</sub> by using ALD process. Figure 20(a) shows the response value of a gas sensor based on 3L WSe<sub>2</sub> to 10 to 500 ppm of NO<sub>2</sub>. When the NO<sub>2</sub> gas concentration reaches 500 ppm, the response is 4140% (figure 20(b)). The sensor has a good recognition effect on different gases. Figure 20(c) shows the response comparison chart of the same concentration of NO<sub>2</sub>, NH<sub>3</sub>, and CO<sub>2</sub> and 10 ppm acetone. It can be seen that 500 ppm of NO<sub>2</sub> has a higher response [90].

Yang *et al* demonstrated a gas sensor based on exfoliated WSe<sub>2</sub> nanosheets, which is used to detect the concentration of trace NO<sub>2</sub> activated by ultraviolet (UV) at 25 °C. NO<sub>2</sub> exhibits high sensitivity under ultraviolet light, with an ultra-low detection limit (LOD) of 8 ppb [91]. Pan *et al* demonstrated a sensor based on a titanium dioxide/tungsten diselenide (TiO<sub>2</sub>/WSe<sub>2</sub>) nanocomposite material, which can sense ethanol with high sensitivity [92]. The sensor has a response of 42.8 in 100 ppm ethanol, as shown in figure 21(a). In a 30 ppm ethanol environment, the response and recovery time is 2 s and 1 s, respectively, which is shown in figure 21(b).

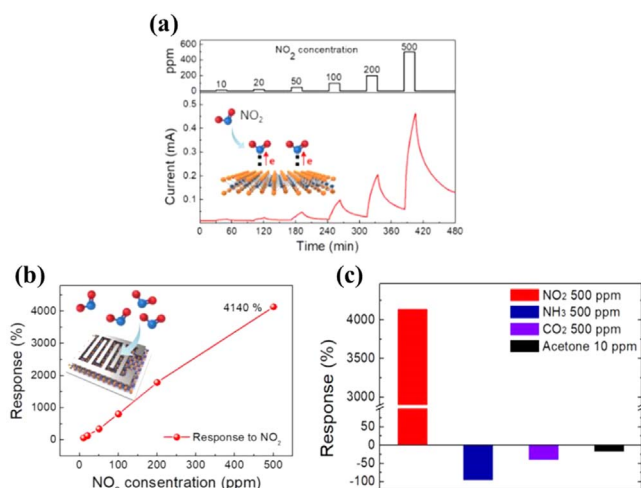


**Figure 20.** (a) Schematic diagram of the response of 3L WSe<sub>2</sub> gas sensor to 10, 20, 50, 100, 200, 500 ppm NO<sub>2</sub>. (b) Response to NO<sub>2</sub> exposure of a 3L WSe<sub>2</sub> gas sensor. (c) The schematic diagram of the WSe<sub>2</sub> gas sensor's response to 500 ppm NO<sub>2</sub>, NH<sub>3</sub>, CO<sub>2</sub> and 10 ppm acetone. Reprinted with permission from [90]. Copyright © 2018, American Chemical Society.

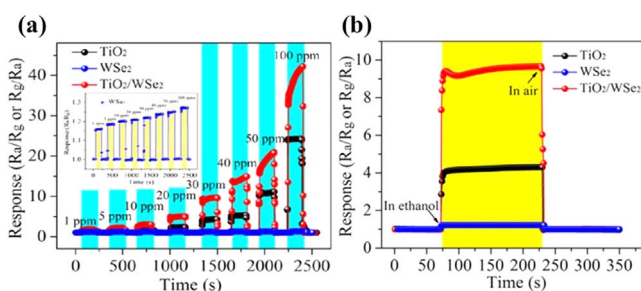


**Figure 21.** (a) The response of TiO<sub>2</sub>/WSe<sub>2</sub>, WSe<sub>2</sub> and TiO<sub>2</sub> thin film sensors to different concentrations of ethanol. (b) Sensing performance of TiO<sub>2</sub>/WSe<sub>2</sub> sensor to 30 ppm ethanol gas. Reprinted from [92], © 2020 Elsevier B.V. All rights reserved.

Baek *et al* reported a multi-layer MoSe<sub>2</sub> FET with NO<sub>2</sub> gas sensing based on CVD fabrication process [93]. The sensor has high sensitivity, real-time response and fast switching characteristics. For 300 ppm of NO<sub>2</sub>, sensitivity is approximately 1907. Furthermore, FET-based sensors and diode-like MoSe<sub>2</sub> sensors were compared, and the use of negative gate voltage can significantly improve sensitivity, indicating the advantages of using FET-based chemical gas sensors [93].

Chen *et al* used a liquid phase exfoliation synthesis method to exfoliate bulk MoSe<sub>2</sub> into nanosheets and fabricated gas sensors [94]. The stripped few-layer MoSe<sub>2</sub> nanosheets showed a good response to NO<sub>2</sub> gas. The response rate at 10 ppm NO<sub>2</sub> was 1500%, which was 18 times higher than that of the original bulk MoSe<sub>2</sub>. The gas sensing device can also detect lower concentrations of NO<sub>2</sub> (50 ppb) [94].

Zhang *et al* showed an ammonia sensor based on MoSe<sub>2</sub> decorated with Pd [95]. When MoSe<sub>2</sub> and Pd-MoSe<sub>2</sub> sensors are exposed to 50 ppm NH<sub>3</sub>, the responses of Pd-MoSe<sub>2</sub> and MoSe<sub>2</sub> sensors are 7.58 and 2.79, respectively. The

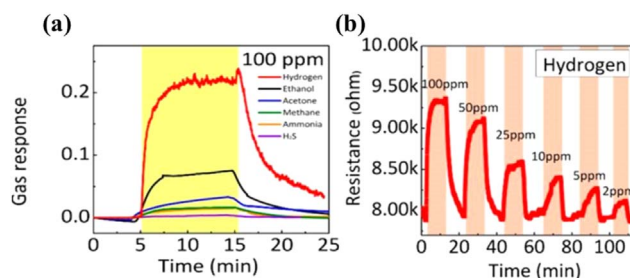


**Figure 22.** (a) The response of the V<sub>2</sub>CT<sub>x</sub> gas sensor to 100 ppm of different gases at room temperature. (b) The response of the gas sensor to different concentrations of hydrogen. Reprinted with permission from [101]. Copyright © 2019, American Chemical Society.

Pd-MoSe<sub>2</sub> sensor has a response time of 130 s, which is significantly faster than the MoSe<sub>2</sub> sensor.

Wu *et al* demonstrated a p-type MoTe<sub>2</sub> gas sensor in which MoTe<sub>2</sub> is obtained by mechanical exfoliation [93]. Under 254 nm ultraviolet radiation, the sensor's sensitivity to NO<sub>2</sub> was significantly increased, resulting in a significantly lower detection limit of 252 ppt [96].

Lastly, it is also worth to mention that, in addition to TMDs, other metal chalcogenides can also be used in gas sensors, such as SnSe<sub>2</sub> [97], V-GaSe [98], In<sub>2</sub>Se<sub>3</sub> [99], and so forth.

#### 4.3. MXenes

Kim *et al* showed that a gas sensor made of Ti<sub>3</sub>C<sub>2</sub>T<sub>x</sub> based on 2D metal carbide MXenes material has a very low detection limit (50–100 ppb) of VOC gas at room temperature [100]. Furthermore, the Ti<sub>3</sub>C<sub>2</sub>T<sub>x</sub> gas sensor also responds to gases such as NO<sub>2</sub>, SO<sub>2</sub> and CO<sub>2</sub>. During N<sub>2</sub> introduction, measuring the average resistance fluctuation can be used to get electrical noise for calculate the signal-to-noise ratios (SNR) of sensors. The calculated noise levels of BP, MoS<sub>2</sub>, RGO and Ti<sub>3</sub>C<sub>2</sub>T<sub>x</sub> are about 1.5%, 1.0%, 0.02% and 0.005%, respectively, and Ti<sub>3</sub>C<sub>2</sub>T<sub>x</sub> has the lowest noise level. After passing 100 ppm of ethanol, ammonia, acetone and propanal, the researchers compared the SNR values of Ti<sub>3</sub>C<sub>2</sub>T<sub>x</sub>, MoS<sub>2</sub>, RGO and BP sensors. For acetone, ethanol, and propanal, the SNR values of Ti<sub>3</sub>C<sub>2</sub>T<sub>x</sub> are 236, 351, and 177, respectively, which are 34, 33, and 54 times of the maximum SNR of other 2D materials. After experimental comparison, the SNR value of Ti<sub>3</sub>C<sub>2</sub>T<sub>x</sub> to ammonia is 3.8 times that of BP, reaching 160 [100].

V<sub>2</sub>CT<sub>x</sub>, another MXene material, can also be used as a gas sensor material. Lee *et al* demonstrated the sensing performance of the V<sub>2</sub>CT<sub>x</sub> gas sensor for non-polar gases [101]. The gas sensor can respond to a variety of gases, as shown in figure 22(a). The detection limit can be considered as the lowest concentration of the analyte, which can be reasonably distinguished from noise. The researchers tested the gas sensing performance of the V<sub>2</sub>CT<sub>x</sub> device. The gas sensor has a good response in the concentration range of 2–100 ppm hydrogen, as shown in figure 22(b). It can respond well to hydrogen sulfide with a concentration of 5 ppm. Using



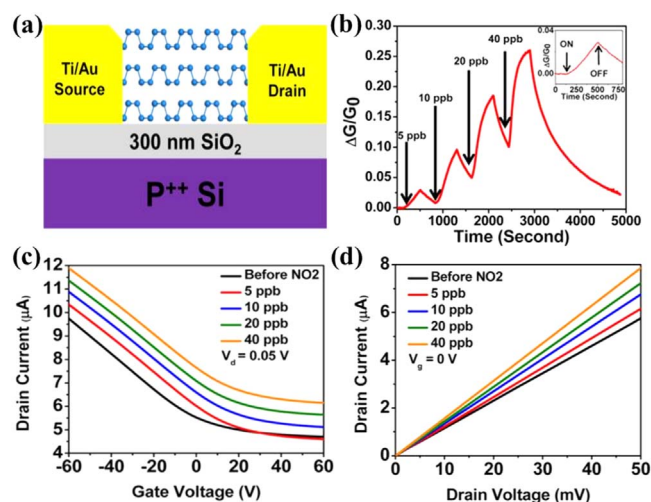


**Figure 23.** (a) Schematic diagram of multilayer BP FET device structure. (b) Conductivity change of BP FET gas sensor in the range of 5–40 ppb  $\text{NO}_2$  concentration. (c)  $I_d$ – $V_g$  curves of multilayer BP FET under different  $\text{NO}_2$  concentration. (d)  $I_d$ – $V_d$  curves of the same device under different  $\text{NO}_2$  concentrations. Reprinted with permission from [103]. Copyright © 2015, American Chemical Society.

theoretical calculations, the theoretical detection limits of  $\text{V}_2\text{CT}_x$  film for methane, hydrogen, acetone and hydrogen sulfide at room temperature are found to be 11.16, 9.39, 1.375, and 3.504 ppm, respectively [101].

Guo *et al* demonstrated a gas sensor based on  $\text{Mo}_2\text{CT}_x$  MXene material [102].  $\text{Mo}_2\text{CT}_x$ -based gas sensing devices are fabricated on Si/ $\text{SiO}_2$  wafers. They grow a 2  $\mu\text{m}$  thick oxide layer through a wet oxidation process, and then deposit interdigital electrodes with a thickness of 280 nm and a pitch of 10  $\mu\text{m}$ . The MXene film is formed by dropping the synthesized  $\text{Mo}_2\text{CT}_x$  suspension on the IDE and drying it overnight in a desiccator. The sensitivity of the sensor at a toluene concentration of 140 ppm is  $0.0366 \Omega \text{ ppm}^{-1}$ , and its detection limit is 220 ppb. In addition to toluene, this gas sensor also shows good sensing capabilities on benzene, ethanol and methanol [102].

#### 4.4. Black phosphorus

As a single-element layered 2D material, black phosphorus (BP) can also be used as the active material in gas sensors. Abbas *et al* demonstrated a  $\text{NO}_2$  gas sensor based on a multilayer BP FET [103]. The device structure is shown in figure 23(a). The BP sensor has relatively high sensitivity and still responds to  $\text{NO}_2$  concentrations as low as 5 ppb, which is shown in figure 23(b). As the concentration of  $\text{NO}_2$  increases, the transfer curves show an obvious upward trend (figure 23(c)). At the same time, output characteristics also show an upward trend, as demonstrated in figure 23(d) [103].

It is worth to mention that, the difference in device structure is also one of the reasons for the change in sensitivity change. Lee *et al* tried for the first time to improve the performance of the BP chemical sensor by floating a BP sheet on top of the electrode column [104]. The suspended BP gas sensor fabricated by dry transfer technique showed higher

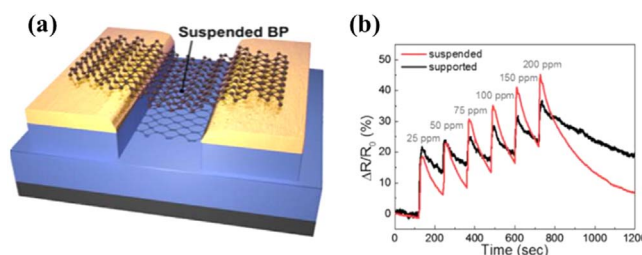


**Figure 24.** (a) Schematic diagram of a suspended BP device. (b) The comparison of response between the supported and suspended BP chemical sensor to  $\text{NO}_2$ . Reprinted from [104], © 2017 Elsevier B.V. All rights reserved.

sensing performance than the traditionally supported BP gas sensor. The structure is shown in figure 24 (a) [104].

At lower gas concentrations, the difference between suspended and supported BP sensors is very small, but it increases as the gas concentration increases (the gas response at 200 ppm increases by 23%), as shown in figure 24(b). The time required for the initial point is approximately twice that of the suspension structure. The tiny gap between the  $\text{SiO}_2$  layer and the BP sheet may affect the desorption process in the supporting device. The suspended BP sensor is expected to have a higher surface area to volume ratio because it can provide additional adsorption sites [92].

It is well known that the BP atomic layer degrades rapidly under environmental conditions, and Jin *et al* demonstrated a BP-based humidity sensor in which the FET is encapsulated with 6 nm thick  $\text{Al}_2\text{O}_3$  [105]. After the humidity sensor was left for seven days, there was almost no change in the sensitivity of humidity [105].

In addition to BP, black arsenene can also be used to make gas sensors that have been theoretically proven to detect  $\text{SO}_2$  in  $\text{SF}_6$  decompositions [106]. Furthermore, other multi-element 2D materials like 2D alloys which consist of three or more elements are also attracting interests for gas sensing applications [107]. Such 2D alloys differs from BP or TMDs, while inheriting the common advantages of vdW materials. Due to the similar high surface area to volume ratio, 2D alloys may have better applications in gas sensing in the future [108].

#### 4.5. 2D heterojunctions

In addition to single 2D materials, 2D material heterojunctions also play an important role in the field of gas sensing. Feng *et al* showed a gas sensor device based on BP/ $\text{MoSe}_2$  heterojunction, and its structure is shown in figure 25(a) [109]. In their work, the gas sensing performance of  $\text{MoSe}_2$  FET, BP FET, and BP/ $\text{MoSe}_2$  heterojunction are comparatively studied. At 200 ppb, the response of heterojunction to  $\text{NO}_2$  is 4.4 times higher than that of  $\text{MoSe}_2$  FET and 46 times than that of BP FET (figure 25(b)). In addition, the lower limit of BP/ $\text{MoSe}_2$  heterojunction detection gas is 10 ppb, which is much lower than  $\text{MoSe}_2$  (60 ppb) and BP (200 ppb) sensors. It is believed that the high sensitivity of the heterojunction gas sensor shown by the experimental results is related to the band alignment modulation at the BP/ $\text{MoSe}_2$  interface.

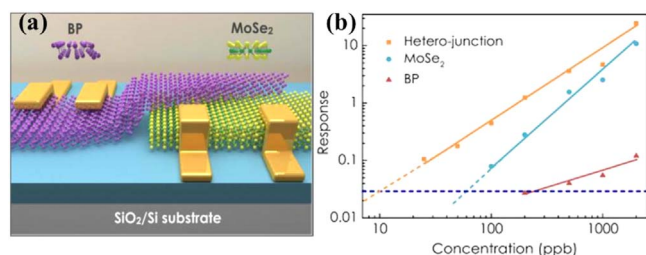


**Figure 25.** (a) Schematic structure of BP/MoSe<sub>2</sub> heterojunction device. (b) All measured concentration responses for MoSe<sub>2</sub> FET, BP FET and heterojunction are plotted on a logarithmic scale. Reproduced from [109]. © IOP Publishing Ltd. All rights reserved.

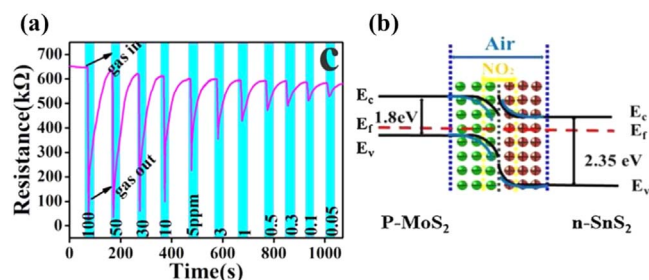


**Figure 26.** (a) Transient dynamic response of the sensor device in an atmosphere of 0.05–100 ppm NO<sub>2</sub>. (b) Compare the band structure of SnS<sub>2</sub>/MoS<sub>2</sub> nanocomposite in air and in NO<sub>2</sub> atmosphere. Reprinted from [110], © 2020 Elsevier B.V. All rights reserved.

Tabata *et al* demonstrated the gas-sensing characteristics of van der Waals heterojunctions based on graphene and MoS<sub>2</sub> flakes [49]. The device is based on FET structure and is composed of graphene and Ti/Au asymmetric contact electrodes on the MoS<sub>2</sub> channel. After exposure to 1 ppm NO<sub>2</sub>, the resistance of the graphene/MoS<sub>2</sub> heterojunction gas sensor changed significantly with a coefficient greater than 10<sup>3</sup>, which is directly related to the Schottky barrier height modulation at the graphene/MoS<sub>2</sub> interface.

Liu *et al* synthesized a new type of heterojunction gas sensors which are composed of flower-like porous SnS<sub>2</sub> nanosheets and MoS<sub>2</sub> nanospheres with exposed edges [110]. The device can detect NO<sub>2</sub> at a minimum of 50 ppb, as shown in figure 26(a). In the heterojunction, electrons are expected to flow from n-type SnS<sub>2</sub> to p-type MoS<sub>2</sub>, which will form an electron depletion layer on the surface of SnS<sub>2</sub>. The SnS<sub>2</sub> surface is expected to receive diffusion of holes from MoS<sub>2</sub> near the p-n interface, resulting in a negatively charged area until a balanced Fermi energy level. When this gas sensor is exposed to NO<sub>2</sub> gas atmosphere, NO<sub>2</sub><sup>-</sup> or NO<sub>3</sub><sup>-</sup> will be generated. This disturbs the balance of the electric field, thereby reducing the barrier width and increasing the conductivity sensor. The band structure of SnS<sub>2</sub>/MoS<sub>2</sub> nanocomposite in air and NO<sub>2</sub> atmosphere is shown in figure 26.

Ikram *et al* synthesized a heterojunction of multi-layer WS<sub>2</sub> and few-layer MoS<sub>2</sub> nanosheets (NSs) and fabricated gas sensors [111]. Multiple devices with different Mo:W atomic ratios are fabricated: MWS-1, MWS-2 and MWS-3 devices with Mo:W atomic ratios of 3.8:1, 1.55:1 and 0.36:1, respectively. The process of synthesizing composite materials is shown in figure 27(a). The MWS-2 gas sensor has good

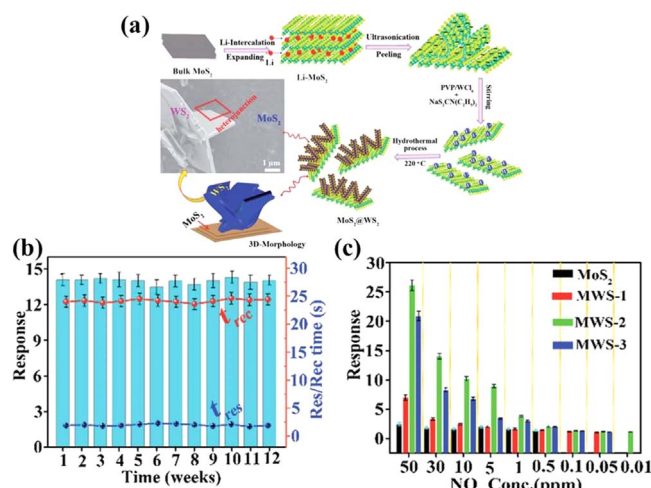


**Figure 27.** (a) Schematic diagram of heterostructure MoS<sub>2</sub>-WS<sub>2</sub> nanocomposite synthesized by one-pot hydrothermal method. (b) Schematic diagram of stability test of MWS-2 gas sensor response to 30 ppm NO<sub>2</sub> in a 12 week period. (c) The response of MoS<sub>2</sub>, MWS-1, MWS-2 and MWS-3 under different concentrations of NO<sub>2</sub>. Reproduced from [111] with permission from the Royal Society of Chemistry.

stability, and the response test to 30 ppm NO<sub>2</sub> in a 12 week period is shown in the figure 27(b). The MWS-2 sensor also achieves the lowest detection limit of 0.01 ppm NO<sub>2</sub>, while pure MoS<sub>2</sub> NSs is 0.5 ppm, MWS-1 is 0.05 ppm, and MWS-3 is 0.05 ppm, which are shown and compared in figure 27(c) [111].

Niu *et al* successfully fabricated a heterojunction based on n-MoS<sub>2</sub>/p-GaSe by mechanical exfoliation and all-dry transfer method [56]. They prepared a photovoltaic self-powered NO<sub>2</sub> gas sensor based on this heterojunction. The heterojunction is exposed to different concentrations of NO<sub>2</sub> under 12 mW cm<sup>-2</sup> and 405 nm light, and observed that the photovoltaic self-powered gas sensor response ranges from 6.3% to 64.3% when the gas concentration is between 20 ppb and 500 ppb. In addition, the heterojunction gas sensor shows good recovery at room temperature [56]. Kumar *et al* demonstrated a gas sensing device made by rGO-MoS<sub>2</sub> hybrids [108]. They used the gas sensor to detect gases such as O<sub>2</sub>, N<sub>2</sub>, and NH<sub>3</sub>. The sensor has the highest sensitivity in NH<sub>3</sub> atmosphere, followed by O<sub>2</sub> with an order of magnitude lower in sensitivity. The sensitivity of the non-reactive gas N<sub>2</sub> is the lowest [112].

Wang *et al* prepared the rGO/WS<sub>2</sub> heterojunction by one-step hydrothermal synthesis and used it to prepare a gas sensing device [113]. The sensor has a 121% response to 10 ppm of NH<sub>3</sub> at 33.5 °C. More importantly, the sensor not only has good long-term stability, but also shows good selectivity to a variety of gases, such as acetone, NO<sub>2</sub>, formaldehyde, benzene, etc, which shows that it can be used as an NH<sub>3</sub> sensor that works at room temperature [113].

Wang *et al* have also fabricated a S-rGO/WS<sub>2</sub> heterojunction by hydrothermal synthesis, in which graphene oxide has been pre-sulfonated in an ice bath [114]. The sulfonation and incorporation of WS<sub>2</sub> nanosheets significantly improved

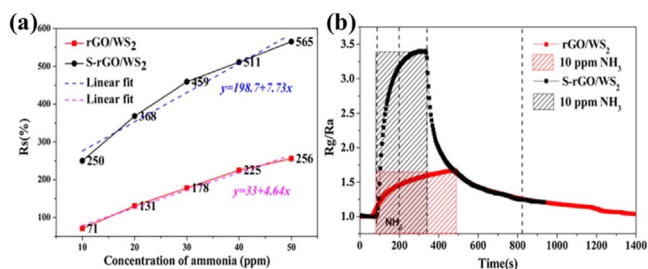


**Figure 28.** (a) Comparison of the difference in ammonia response between rGO/WS<sub>2</sub> and S-rGO/WS<sub>2</sub>. (b) Normalized response curves of S-rGO/WS<sub>2</sub> and rGO/WS<sub>2</sub> in an atmosphere of 10 ppm ammonia. Reprinted from [114], © 2021 Published by Elsevier B.V.

the rGO-based chemical resistance sensor for ammonia sensing performance at room temperature. The response value of S-rGO/WS<sub>2</sub> shows a linear trend with ammonia, as shown in figure 28(a). At room temperature, the response value of S-rGO/WS<sub>2</sub> to NH<sub>3</sub> is twice of the rGO/WS<sub>2</sub>. By comparing the response and recovery time to 10 ppm ammonia, S-rGO/WS<sub>2</sub> shows a much shorter time than rGO/WS<sub>2</sub>, as demonstrated in figure 28(b). The sensor has a 250% response to 10 ppm of NH<sub>3</sub> at 28 °C [114].

Paolucci *et al* demonstrated a WS<sub>2</sub>-modified rGO as a chemical resistance NO<sub>2</sub> film sensor [115]. They compared the NO<sub>2</sub> gas response of a single rGO film and a WS<sub>2</sub>-modified rGO film in dry air with operating temperature at 25 °C and 50 °C. The results are shown in figure 29(a). It is obvious that the rGO film modified by WS<sub>2</sub> has a stronger response to NO<sub>2</sub> gas. They measured the response of a single-layer rGO film and a WS<sub>2</sub> modified rGO film to 1 ppm NO<sub>2</sub> gas under purple blue light at different power densities (270  $\mu\text{W cm}^{-2}$ , 468  $\mu\text{W cm}^{-2}$ , and 668  $\mu\text{W cm}^{-2}$ ), and the results are shown in figure 29(b). The response of WS<sub>2</sub> modified rGO in 1 ppm NO<sub>2</sub> atmosphere is about 1.21 [115].

Choi *et al* produced a tunnel FET based on a graphene/WS<sub>2</sub>/graphene heterostructure [116]. This transistor adjusts the WS<sub>2</sub> barrier as a function of the concentration of gas molecules, demonstrating the rectification behavior of the sensitivity signal. As shown in figure 30, the t-GFET gas sensor consists of two channels: the top (T-SLG) and the bottom SLG (B-SLG), which are vertically separated by the thin WS<sub>2</sub> barrier. In the heterostructure of G/WS<sub>2</sub>/G,  $\Delta E$  causes the Fermi levels of B-SLG and T-SLG to align under equilibrium conditions, which leads to the tilt of the WS<sub>2</sub> tunnel barrier. They found that compared with NH<sub>3</sub> molecules, NO<sub>2</sub> molecules contribute more to the change of  $\Delta I_t/I_t$  when adsorbed on T-SLG [116].

Shi *et al* demonstrated a FET type gas sensor utilizing BP, MoS<sub>2</sub>, and boron nitride (BN) as the top gate, conductive channel, and mid-electric layer, respectively [117]. The separation of sensing and conductive materials can perform better at sensing and realize long-term stability, which are achieved by using distinct materials for gas adsorption and conduction purposes. Among them, the BP top gate is used as a sensing material, and the BN dielectric layer is used to cover the conductive channel of MoS<sub>2</sub> to insulate it from the surrounding environment. The sensor can detect NO<sub>2</sub> up to the

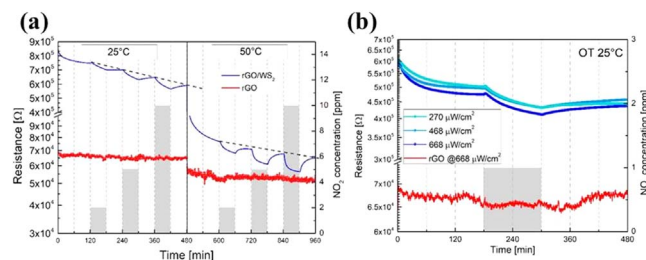


**Figure 29.** (a) Response of a single rGO film and a WS<sub>2</sub>-modified rGO film to 2–10 ppm NO<sub>2</sub> in dry air at 25 °C and 50 °C operating temperature. (b) Response of a single-layer rGO film and a WS<sub>2</sub> modified rGO film to 1 ppm NO<sub>2</sub> gas under purple blue light at different power densities. Reproduced from [115]. CC BY 4.0.

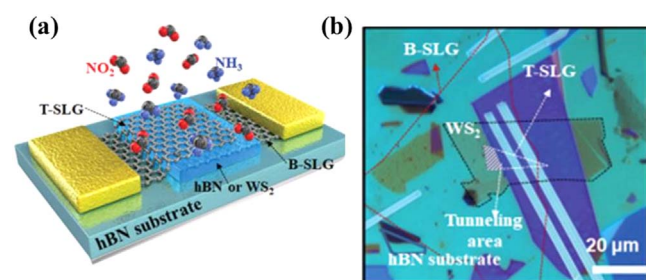


**Figure 30.** (a) Schematic diagram and (b) optical image of tunneling G/hBN/G or G/WS<sub>2</sub>/G FET. Reproduced from [116] with permission from the Royal Society of Chemistry.

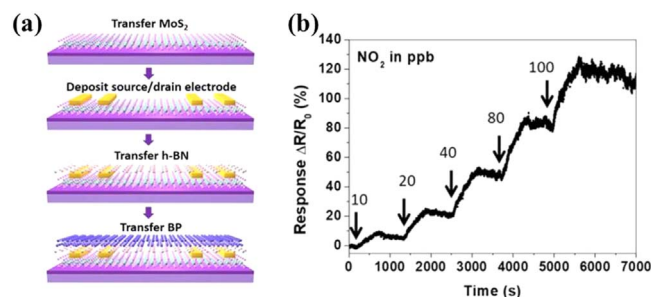


**Figure 31.** (a) The fabrication process of BP/BN/MoS<sub>2</sub> hetero-junction device. (b) Real-time sensing response of the BP/BN/MoS<sub>2</sub> heterojunction device to NO<sub>2</sub>. Reproduced from [117]. © IOP Publishing Ltd. All rights reserved.

ppb level, and the lowest possible detection limit is 3.3 ppb, as shown in figure 31(b) [117].

Afzal *et al* have fabricated a gas sensor based on heterojunction bipolar transistor (HBT). The sensor is mainly composed of n-WS<sub>2</sub>/p-GeSe/n-WS<sub>2</sub> van der Waals (vdW) heterostructure, which is shown in figure 32(a). The collector and emitter of the HBT are both composed of WS<sub>2</sub>, located at the bottom and top of the heterojunction, respectively. In order to better study the performance of the heterojunction HBT, they tested the device performance in common emitter and common base configurations. In order to detect the gas response, they detected the change of the collector current of the device in a gas environment in the common emitter configuration, and studied its influence on the gas-sensing effect by changing the  $V_{CE}$  and  $V_{BE}$ . The response time can be shortened by applying a higher  $V_{CE}$  value, as shown in



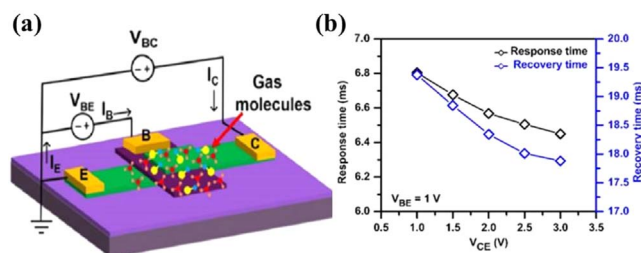


**Figure 32.** (a) Common emitter configuration diagram of 2D-HBT gas sensor device based on n-WS<sub>2</sub>/p-GeSe/n-WS<sub>2</sub>. (b) The response and recovery time of the HBT gas sensor varies with  $V_{CE}$  under a fixed  $V_{BE}$ . Reprinted with permission from [118]. Copyright © 2020, American Chemical Society.

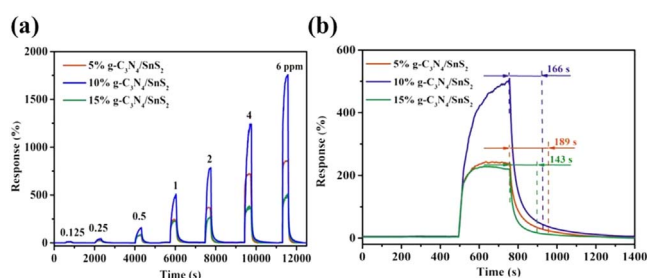


**Figure 33.** (a) The dynamic sensing performance of 5%, 10%, and 15% g-C<sub>3</sub>N<sub>4</sub>/SnS<sub>2</sub> to NO<sub>2</sub> changes as the concentration increases from 0.125 to 6 ppm. (b) Response and recovery curves of 5%, 10%, and 15% g-C<sub>3</sub>N<sub>4</sub>/SnS<sub>2</sub> sensors to 1 ppm NO<sub>2</sub>. Reproduced from [119]. © IOP Publishing Ltd. All rights reserved.

figure 32(b). Another effective way to reduce the response time is to dope the emitter, which is essential for generating a large number of charge carriers [118].

Sun *et al* combined SnS<sub>2</sub> and g-C<sub>3</sub>N<sub>4</sub> nanosheets to form a 2D/2D heterojunction, which increased adsorption sites and enhanced charge transfer [119]. Because of the high resistivity and weak adsorption of NO<sub>2</sub>, the original SnS<sub>2</sub> fails in working at room temperature, while the g-C<sub>3</sub>N<sub>4</sub>/SnS<sub>2</sub> heterojunction shows an ultra-high response (503%) and short recovery time (166 s) to 1 ppm NO<sub>2</sub> at room temperature. They used 5%, 10%, and 15% g-C<sub>3</sub>N<sub>4</sub>/SnS<sub>2</sub> to verify that as the mass ratio decreases, the recovery time continues to decrease, which is shown in figure 33.

Kuchi *et al* explored the ethanol gas response of different PbS:SnS<sub>2</sub> material ratios (1:0, 1:1, 1:2, 1:3, 0:1, 2:1, and 3:1) [120]. It is concluded that the sensor based on PbS:SnS<sub>2</sub> (1:1) shows the best ethanol gas sensing performance. They further used the sensor based on PbS:SnS<sub>2</sub> (1:1) to detect ethanol, methane, CO, CO<sub>2</sub>, O<sub>2</sub>, and acetone and methanol. The response to ethanol is much greater than to several other gases. At room temperature, the sensor responsivity to 60–1600 ppm ethanol gas is 45.64%–100.3% [120].

Wu *et al* demonstrated a 3D structure heterojunction that combines the advantages of RGO and SnS<sub>2</sub> [121]. The heterojunction is synthesized by hydrothermal method. Original graphene shows poor performance in NO<sub>2</sub> detection because of its poor selectivity. Although SnS<sub>2</sub> shows a strong physical affinity for NO<sub>2</sub>, its practicality is limited by the ultra-high resistance and low sensitivity at room temperature. In their

work, the flexible porous LCP substrate enables the NO<sub>2</sub> sensor to work in a highly curved state without sacrificing its sensitivity. The responses of RGO and SnS<sub>2</sub>/RGO sensors to 8 ppm NO<sub>2</sub> were 2.2% and 49.8%. It shows that the response of RGO modified by SnS<sub>2</sub> increased by 22.6 times. Due to the strong physical affinity of SnS<sub>2</sub> and RGO to NO<sub>2</sub>, the effective charge transfer is promoted by the depletion layer formed at the heterojunction interface, and the abundant adsorption sites are the main reasons for their high sensitivity [121]. Luo *et al* demonstrated an ammonia (NH<sub>3</sub>) gas sensor based on WS<sub>2</sub>/CuO heterojunction. The low sensitivity of WS<sub>2</sub> NSs to ammonia gas was ameliorated by functionalization with CuO nanoparticles [122].

In addition to 2D material heterojunctions, 2D material homojunctions can also be used in gas sensing applications. Garam *et al* demonstrated a graphene-CPG-graphene homojunction-based gas sensor, in which the chemically patterned graphene was mainly achieved by high-energy electron irradiation. In terms of NO<sub>2</sub> gas sensing performance, the graphene-CPG-graphene homojunction gas sensor improves the sensing performance by 839% compared with the pristine graphene-based gas sensor [123].

Zheng *et al* demonstrated a MoS<sub>2</sub> homojunction-based gas sensor. The gas sensor is formed by stacking n-type CVD MoS<sub>2</sub> and p-type MoS<sub>2</sub> synthesized by soft chemical route. Compared with the p-type MoS<sub>2</sub> sensor, the p-n junction homojunction MoS<sub>2</sub> gas sensor is 60 times more sensitive to 20 ppm NO<sub>2</sub>. In addition, the gas sensor can be fully recovered within 30 s by UV irradiation [124]. From the recent studies, 2D junction devices have provided a promising device platform for the realization of various sensing technologies [125, 126].

#### 4.6. 2D metal oxides

Besides traditional 2D materials, other materials with 2D structure like 2D metal oxides also have good applications in gas sensors. Khan *et al* demonstrated a 2D tungsten oxide-based gas sensor that primarily uses wet-chemical synthesis techniques. The gas sensing device annealed at 225 °C showed good sensitivity to NO<sub>2</sub> gas at operating temperature 150 °C (figure 34(a)). In addition, the gas sensor has also been shown to have good NO<sub>2</sub> selectivity in various gases such as H<sub>2</sub>, H<sub>2</sub>S, NH<sub>3</sub>, and so forth (figure 34(b)). The magnetic dipole formed by NO<sub>2</sub> on the nearby tungsten oxide and the selected crystal orientation are considered to be the reasons for the good selectivity of NO<sub>2</sub> gas [127].

2D nanosheet materials require higher operating temperatures in gas sensing applications. To improve this, the researchers explored the feasibility of 2D nanosheet material systems integrated with optical fibers for gas sensing at room temperature. Liu *et al* demonstrated a gas sensor based on ZnO-Bi<sub>2</sub>O<sub>3</sub> NSs, which was realized *in situ* on the surface of HCF by sol-gel and hydrothermal processes [128]. The sensor shows low acetone concentration gas sensing in the range of 0–100 ppm at room temperature.

So far, 2D materials have shown great advantages in gas sensing applications, both in terms of responsivity and

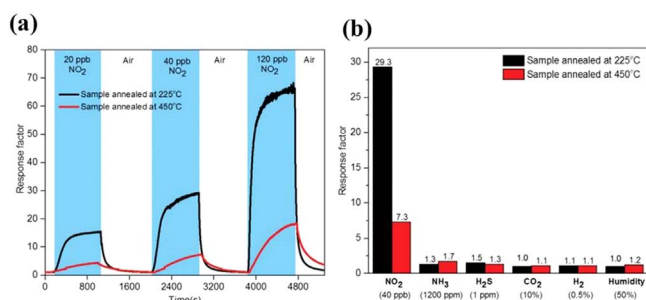


**Figure 34.** (a) Dynamic responses to NO<sub>2</sub> based on two gas sensors at different annealing temperatures (225 °C and 450 °C). (b) Selective measurements of H<sub>2</sub> (0.5%), H<sub>2</sub>S (1 ppm), NH<sub>3</sub> (1200 ppm), NO<sub>2</sub> (40 ppb), CO<sub>2</sub> (10%) and humidity (50%) based on two gas sensors at different annealing temperatures. Reproduced from [127] with permission from the Royal Society of Chemistry.

selectivity. However, gas sensing devices based on 2D materials are still relatively simple in structure, and the reliability and reproducibility still remain a bottleneck. Further materials optimization and device engineering in advanced gas sensing applications may shed more light on this issue discussed above.

## 5. Summary and perspectives

This review mainly focuses on the 2D material-based gas sensors. It mainly introduces the types of sensors, the sensing principle of gas sensors, and the development process of 2D materials in the field of gas sensing. The large surface-to-volume ratio makes the 2D materials and the homo-/heterojunctions promising in gas sensing device implementation. By using mechanical lift-off methods, CVD growth methods, and so on, good semiconducting or conductivity properties can be achieved from the 2D material families, which provide a good way to fabricate resistor-type or other non-resistor-type devices towards low-power and high-sensitivity gas sensing applications. At present, 2D material-based gas sensors have been fabricated on both rigid and flexible substrates, which make them more attractive for future heterostructure integration applications.

In order to further improve the performance of 2D material gas sensors, the following methods are mainly utilized: 1. using different metals to modify 2D materials to improve the sensing sensitivity; 2. synthesis of 2D structure materials like metal oxides; 3. synthesis of 2D materials and organic compounds; 4. 2D material heterojunction gas sensors use the depletion layer formed at the interface of the heterojunction to promote effective charge transfer; 5, the use of gate control and other transistor characteristics to improve gas sensitivity.

Based on the above methods to improve sensitivity, it may be a good research focus to combine transistor performance with gas sensing. On the basis of the same material, the purpose of improving the sensitivity may be achieved by optimizing the performance of the transistor. In addition, 2D composite gas sensors may still be a promising research direction. With the deepening of 2D materials research,

combining different materials is expected to achieve better sensitivity, selectivity, and stability. Furthermore, gas sensing can be further implemented in intelligent systems, using algorithms for gas reorganization and discrimination purposes.

## Acknowledgments

This work was supported by the Science and Technology Commission of Shanghai Municipality (20501130202), the Open Research Fund of State Key Laboratory of Bioelectronics, Southeast University, and the young scientist project of MOE innovation platform.

## Data availability statement

The data that support the findings of this study are available upon reasonable request from the authors.

## ORCID iDs

Lin Chen <https://orcid.org/0000-0002-7145-7564>

Hao Zhu <https://orcid.org/0000-0003-3890-6871>

## References

- [1] Shang W *et al* 2021 Rotational pulsed triboelectric nanogenerators integrated with synchronously triggered mechanical switches for high efficiency self-powered systems *Nano Energy* **82** 105725
- [2] Zhang S *et al* 2022 The self-powered artificial synapse mechanotactile sensing system by integrating triboelectric plasma and gas-ionic-gated graphene transistor *Nano Energy* **91** 106660
- [3] Liu X, Cui P, Wang J, Shang W, Zhang S, Guo J, Gu G, Zhang B, Cheng G and Du Z 2021 A robust all-inorganic hybrid energy harvester for synergistic energy collection from sunlight and raindrops *Nanotechnology* **32** 075401
- [4] Nasiri N and Clarke C 2019 Nanostructured gas sensors for medical and health applications: low to high dimensional materials *Biosensors* **9** 43
- [5] Panneerselvam G, Thirumal V and Pandya H M 2018 Review of surface acoustic wave sensors for the detection and identification of toxic environmental gases/vapours *Arch. Acoust.* **43** 357–67
- [6] Muruganandham M, Zhang Y F, Suri R, Lee G J, Chen P K, Hsieh S H, Sillanpaa M and Wu J J 2015 Environmental applications of ZnO materials *J. Nanosci. Nanotechnol.* **15** 6900–13
- [7] Liu J J, Chen G, Yu Y G, Wu Y L, Zhou M J, Zhang H Q, Lv C D, Qin H and Qi X 2016 Template-free preparation of mesoporous single crystal In<sub>2</sub>O<sub>3</sub> achieving superior ethanol gas sensing performance *RSC Adv.* **6** 14615–9
- [8] Chang G and Xu M 2013 Research progress and potential application of WO<sub>3</sub> electrochromic films *Int. Conf. on Advances and Trends in Engineering Materials and Their Applications (ATEMA 2013)* pp 373–9

- [9] Adamyan A Z, Adamian Z N and Aroutiounian V M 2003 Preparation of SnO<sub>2</sub> films with thermally stable nanoparticles *Sensors* **3** 438–42
- [10] Macak J M, Tsuchiya H, Ghicov A, Yasuda K, Hahn R, Bauer S and Schmuki P 2007 TiO<sub>2</sub> nanotubes: self-organized electrochemical formation, properties and applications *Curr. Opin. Solid State Mater. Sci.* **11** 3–18
- [11] Zhang L, Khan K, Zou J F, Zhang H and Li Y C 2019 Recent advances in emerging 2D material-based gas sensors: potential in disease diagnosis *Adv. Mater. Interfaces* **6** 1901329
- [12] Novoselov K S, Geim A K, Morozov S V, Jiang D, Zhang Y, Dubonos S V, Grigorieva I V and Firsov A A 2004 Electric field effect in atomically thin carbon films *Science* **306** 666–9
- [13] Shen C and Oyadiji S O 2020 The processing and analysis of graphene and the strength enhancement effect of graphene-based filler materials: a review *Mater. Today Phys.* **15** 100257
- [14] Yoon H W, Cho Y H and Park H B 2016 Graphene-based membranes: status and prospects *Phil. Trans. R. Soc. A* **374** 20150024
- [15] Gao X Y, Yao Y and Meng X C 2020 Recent development on BN-based photocatalysis: a review *Mater. Sci. Semicond. Process.* **120** 105256
- [16] Yadav V and Kulshrestha V 2019 Boron nitride: a promising material for proton exchange membranes for energy applications *Nanoscale* **11** 12755–73
- [17] Qiao Y C, Hirtz T, Wu F, Deng G, Li X S, Zhi Y, Tian H, Yang Y and Ren T L 2020 Fabricating molybdenum disulfide memristors *ACS Appl. Electron. Mater.* **2** 346–70
- [18] Zhang X, Lai Z C, Tan C L and Zhang H 2016 Solution-processed two-dimensional MoS<sub>2</sub> nanosheets: preparation, hybridization, and applications *Angew. Chem.—Int. Ed.* **55** 8816–38
- [19] Sethulekshmi A S, Jayan J S, Saritha A and Joseph K 2021 Insights into the reforcibility and multifarious role of WS<sub>2</sub> in polymer matrix *J. Alloys Compd.* **876** 160107
- [20] Lan C Y, Li C, Ho J C and Liu Y 2021 2D WS<sub>2</sub>: from vapor phase synthesis to device applications *Adv. Electron. Mater.* **7** 2000688
- [21] Xu L P, Zhou J X, He Z, Hu J B and Liu M R 2021 Large area chemical vapor deposition and spectroscopic properties of bilayer WSe<sub>2</sub> *Mater. Lett.* **284** 128994
- [22] Liu B L, Fathi M, Chen L, Abbas A, Ma Y Q and Zhou C W 2015 Chemical vapor deposition growth of monolayer WSe<sub>2</sub> with tunable device characteristics and growth mechanism study *ACS Nano* **9** 6119–27
- [23] Joshi N, Hayasaka T, Liu Y M, Liu H L, Oliveira O N and Lin L W 2018 A review on chemiresistive room temperature gas sensors based on metal oxide nanostructures, graphene and 2D transition metal dichalcogenides *Microchim. Acta* **185** 213
- [24] Cui J, Li P, Wang H, Qu F and Liu Z 2020 Recent progress in two-dimensional transition metaldichalcogenides *Chin. J.* **65** 882–903
- [25] Lee E and Kim D J 2019 Review-recent exploration of two-dimensional MXenes for gas sensing: from a theoretical to an experimental view *J. Electrochem. Soc.* **167**
- [26] Luo W J, Yang R, Liu J L, Zhao Y L, Zhu W J and Xia G R 2017 Thermal sublimation: a scalable and controllable thinning method for the fabrication of few-layer black phosphorus *Nanotechnology* **28** 285301
- [27] Sinha S, Takabayashi Y, Shinohara H and Kitaura R 2016 Simple fabrication of air-stable black phosphorus heterostructures with large-area hBN sheets grown by chemical vapor deposition method *2D Mater.* **3** 035010
- [28] Khan M S, Srivastava A and Pandey R 2016 Electronic properties of a pristine and NH<sub>3</sub>/NO<sub>2</sub> adsorbed buckled arsenene monolayer *RSC Adv.* **6** 72634–42
- [29] Wu J Q *et al* 2020 Antimonene nanosheets fabricated by laser irradiation technique with outstanding nonlinear absorption responses *Appl. Phys. Lett.* **116** 261903
- [30] Grazianetti C, Martella C and Molle A 2020 The xenes generations: a taxonomy of epitaxial single-element 2D materials *Phys. Status Solidi-Rapid Res. Lett.* **14** 1900439
- [31] Wang C X, Yin L W, Zhang L Y, Xiang D and Gao R 2010 Metal oxide gas sensors: sensitivity and influencing factors *Sensors* **10** 2088–106
- [32] Yang S L, Lei G, Xu H X, Lan Z G, Wang Z and Gu H S 2021 Metal oxide based heterojunctions for gas sensors: a review *Nanomaterials* **11** 1026
- [33] Kim H J and Lee J H 2014 Highly sensitive and selective gas sensors using p-type oxide semiconductors: overview *Sensors Actuators B* **192** 607–27
- [34] Hu Y, Zhou X H, Han Q, Cao Q X and Huang Y X 2003 Sensing properties of CuO–ZnO heterojunction gas sensors *Mater. Sci. Eng. B* **99** 41–3
- [35] Kim J, Kim W and Yong K 2012 CuO/ZnO heterostructured nanorods: photochemical synthesis and the mechanism of H<sub>2</sub>S gas sensing *J. Phys. Chem. C* **116** 15682–91
- [36] Xu Q, Ju D X, Zhang Z C, Yuan S, Zhang J, Xu H Y and Cao B Q 2016 Near room-temperature triethylamine sensor constructed with CuO/ZnO P–N heterostructural nanorods directly on flat electrode *Sensors Actuators B* **225** 16–23
- [37] Hu J *et al* 2018 Synthesis and gas sensing properties of NiO/SnO<sub>2</sub> hierarchical structures toward ppb-level acetone detection *Mater. Res. Bull.* **102** 294–303
- [38] Ju D X, Xu H Y, Xu Q, Gong H B, Qiu Z W, Guo J, Zhang J and Cao B Q 2015 High triethylamine-sensing properties of NiO/SnO<sub>2</sub> hollow sphere P–N heterojunction sensors *Sensors Actuators B* **215** 39–44
- [39] Liu H C, Wang F P, Hu K L, Zhang B, He L and Zhou Q 2019 Superior hydrogen sensing property of porous NiO/SnO<sub>2</sub> nanofibers synthesized via carbonization *Nanomaterials* **9** 1250
- [40] Meng D, Liu D Y, Wang G S, Shen Y B, San X G, Li M and Meng F L 2018 Low-temperature formaldehyde gas sensors based on NiO–SnO<sub>2</sub> heterojunction microflowers assembled by thin porous nanosheets *Sensors Actuators B* **273** 418–28
- [41] Yue Q, Shao Z Z, Chang S L and Li J B 2013 Adsorption of gas molecules on monolayer MoS<sub>2</sub> and effect of applied electric field *Nanoscale Res. Lett.* **8** 425
- [42] Wang T X, Zhao R M, Zhao X, An Y P, Dai X Q and Xia C X 2016 Tunable donor and acceptor impurity states in a WSe<sub>2</sub> monolayer by adsorption of common gas molecules *RSC Adv.* **6** 82793–800
- [43] Kim Y *et al* 2020 2D transition metal dichalcogenide heterostructures for p- and n-type photovoltaic self-powered gas sensor *Adv. Funct. Mater.* **30** 2003360
- [44] Li B L, Chen X W, Su C, Han Y T, Wang H Z, Zeng M, Wang Y, Liang T, Yang Z and Xu L 2020 Enhanced dimethyl methylphosphonate detection based on two-dimensional WSe<sub>2</sub> nanosheets at room temperature *Analyst* **145** 8059–67
- [45] Acharyya S, Nag S, Kimbature S, Ghose A, Pal A and Guha P K 2021 Selective discrimination of VOCs applying gas sensing kinetic analysis over a metal oxide-based chemiresistive gas sensor *ACS Sens.* **6** 2218–24
- [46] Smith M K, Jensen K E, Pivak P A and Mirica K A 2016 Direct self-assembly of conductive nanorods of metal-organic frameworks into chemiresistive devices on shrinkable polymer films *Chem. Mater.* **15** 5264–8



- [47] Jung G, Hong S, Jeong Y, Shin W, Park J, Kim D, Bae J H, Park B G and Lee J H 2021 Response comparison of resistor- and Si FET-type gas sensors on the same substrate *IEEE Trans. Electron Devices* **68** 3552–7
- [48] Shin W, Jung G, Hong S, Jeong Y, Park J, Jang D, Park B-G and Lee J-H 2020 Low frequency noise characteristics of resistor- and Si MOSFET-type gas sensors fabricated on the same Si wafer with In<sub>2</sub>O<sub>3</sub> sensing layer *Sensors Actuators B* **318** 128087
- [49] Tabata H, Matsuyama H, Goto T, Kubo O and Katayama M 2021 Visible-light-activated response originating from carrier-mobility modulation of NO<sub>2</sub> gas sensors based on MoS<sub>2</sub> monolayers *ACS Nano* **15** 2542–2553
- [50] Hazra A 2020 Amplified methanol sensitivity in reduced graphene oxide FET using appropriate gate electrostatic *IEEE Trans. Electron Devices* **67** 5111–8
- [51] Ricciardella F, Nigro M A, Miscioscia R, Miglietta M L and Polichetti T 2021 Investigation of multi-layered graphene/silicon Schottky junction in oxidizing atmosphere *J. Phys. D: Appl. Phys.* **54** 375104
- [52] Kim Y, Kang S-K, Oh N-C, Lee H-D, Lee S-M, Park J and Kim H 2019 Improved sensitivity in schottky contacted two-dimensional MoS<sub>2</sub> gas sensor *ACS Appl. Mater. Interfaces* **11** 38902–9
- [53] Mahmoodnia H, Salehi A and Mastelaro V R 2021 Enhancement of ammonia gas sensing properties of GaAs-based schottky diodes using ammonium sulfide surface passivation *IEEE Sens. J.* **21** 4209–15
- [54] Yang S X, Jiang C B and Wei S H 2017 Gas sensing in 2D materials *Appl. Phys. Rev.* **4** 021304
- [55] Luther B P, Wolter S D and Mohney S E 1999 High temperature Pt Schottky diode gas sensors on n-type GaN *Sensors Actuators B* **56** 164–8
- [56] Niu Y, Zeng J W, Liu X C, Li J L, Wang Q, Li H, de Rooij N F, Wang Y and Zhou G F 2021 A photovoltaic self-powered gas sensor based on all-dry transferred MoS<sub>2</sub>/GaSe heterojunction for ppb-level NO<sub>2</sub> sensing at room temperature *Adv. Sci.* **8** 210047
- [57] Dhara S, Jawa H, Ghosh S, Varghese A, Karmakar D and Lodha S 2021 All-electrical high-sensitivity, low-power dual-mode gas sensing and recovery with a WSe<sub>2</sub>/MoS<sub>2</sub> pn heterodiode *ACS Appl. Mater. Interfaces* **13** 30785–96
- [58] Tang H, Sacco L N, Vollebregt S, Ye H, Fan X and Zhang G 2020 Recent advances in 2D/nanostructured metal sulfides-based gas sensors: mechanisms, applications, and perspectives *J. Mater. Chem. A* **8** 24943–76
- [59] Yoo B K, Park Y W, Kang C Y, Yoon S J and Kim J S 2006 Surface acoustic wave sensors to detect volatile gases by measuring output phase shift *J. Electroceram.* **17** 1013–7
- [60] Jakubik W P 2011 Surface acoustic wave-based gas sensors *Thin Solid Films* **520** 986–93
- [61] Luo J T, Feng X Y, Kan H, Li H and Fu C 2021 One-dimensional Bi<sub>2</sub>S<sub>3</sub> nanobelts-based surface acoustic wave sensor for NO<sub>2</sub> detection at room temperature *IEEE Sens. J.* **21** 1404–8
- [62] Rheaume J M and Pisano A P 2011 A review of recent progress in sensing of gas concentration by impedance change *Ionics* **17** 99–108
- [63] Cvejin K, Manjakkal L, Kulawik J, Zaraska K and Szwagierczak D 2015 Planar impedancemetric NO sensor with thick film perovskite electrodes based on samarium cobaltite *Electroanalysis* **27** 760–9
- [64] Shimizu Y, Yamamoto S and Takase S 2017 A thick-film impedancemetric carbon monoxide sensor using layered perovskite-type cuprate *Sensors Actuators B* **249** 667–72
- [65] Martin L P, Woo L Y and Glass R S 2007 Impedancemetric NO<sub>x</sub> sensing using YSZ electrolyte and YSZ/Cr<sub>2</sub>O<sub>3</sub> composite electrodes *J. Electrochem. Soc.* **154** J97–104
- [66] Nakatou M and Miura N 2004 Impedancemetric sensor based on YSZ and In<sub>2</sub>O<sub>3</sub> for detection of low concentrations of water vapor at high temperature *Electrochem. Commun.* **6** 995–8
- [67] Schedin F, Geim A K, Morozov S V, Hill E W, Blake P, Katsnelson M I and Novoselov K S 2007 Detection of individual gas molecules adsorbed on graphene *Nat. Mater.* **6** 652–5
- [68] Hwang S, Lim J, Park H G, Kim W K, Kim D H, Song I S, Kim J H, Lee S, Woo D H and Jun S C 2012 Chemical vapor sensing properties of graphene based on geometrical evaluation *Curr. Appl. Phys.* **12** 1017–22
- [69] Chung M G, Kim D H, Lee H M, Kim T, Choi J H, Seo D K, Yoo J B, Hong S H, Kang T J and Kim Y H 2012 Highly sensitive NO<sub>2</sub> gas sensor based on ozone treated graphene *Sensors Actuators B* **166** 172–6
- [70] Choi H *et al* 2014 Flexible and transparent gas molecule sensor integrated with sensing and heating graphene layers *Small* **10** 3685–91
- [71] Sundaram R S, Gómez-Navarro C, Balasubramanian K, Burghard M and Kern K 2008 Electrochemical modification of graphene *Adv. Mater.* **20** 3050–3
- [72] Lo C F, Nicolosi J, Chang C Y, Chen V, Strupinski W, Pearton S J and Ren F 2011 Hydrogen detection using platinum coated graphene grown on SiC *Sensors Actuators B* **157** 500–3
- [73] Johnson J L, Behnam A, Pearton S J and Ural A 2010 Hydrogen sensing using pd-functionalized multi-layer graphene nanoribbon networks *Adv. Mater.* **22** 4877–80
- [74] Ovsianyskyi O, Nam Y S, Tsymbalenko O, Lan P T, Moon M W and Lee K B 2018 Highly sensitive chemiresistive H<sub>2</sub>S gas sensor based on graphene decorated with Ag nanoparticles and charged impurities *Sensors Actuators B* **257** 278–85
- [75] Liang S, Zhu J, Ding J, Bi H, Yao P, Han Q and Wang X 2015 Deposition of cocoon-like ZnO on graphene sheets for improving gas-sensing properties to ethanol *Appl. Surf. Sci.* **357** 1593–600
- [76] Wu J *et al* 2020 Metal–organic framework for transparent electronics *Adv. Sci.* **7** 1903003
- [77] Jang A R, Lim J E, Jang S, Kang M H, Lee G, Chang H, Kim E, Park J K and Lee J O 2021 Ag<sub>2</sub>S nanoparticles decorated graphene as a selective chemical sensor for acetone working at room temperature *Appl. Surf. Sci.* **562** 150201
- [78] Eom W, Jang J S, Lee S H, Lee E, Jeong W, Kim I D, Choi S J and Han T H 2021 Effect of metal/metal oxide catalysts on graphene fiber for improved NO<sub>2</sub> sensing *Sensors Actuators B* **344** 130231
- [79] Zhang X X, Teng S Y, Loy A C M, How B S, Leong W D and Tao X T 2020 Transition metal dichalcogenides for the application of pollution reduction: a review *Nanomaterials* **10** 1012
- [80] Liu B, Chen L, Liu G, Abbas A N, Fathi M and Zhou C 2014 High-performance chemical sensing using Schottky-contacted chemical vapor deposition grown monolayer MoS<sub>2</sub> transistors *ACS Nano* **8** 5304
- [81] Kumar R, Goel N and Kumar M 2017 UV-activated MoS<sub>2</sub> based fast and reversible NO<sub>2</sub> sensor at room temperature *ACS Sens.* **11** 1744–52
- [82] Li H, Yin Z, He Q, Li H, Huang X, Lu G, Fam D W H, Tok A I Y, Zhang Q and Zhang H 2012 Fabrication of single- and multilayer MoS<sub>2</sub> film-based field-effect transistors for sensing NO at room temperature *Small* **8** 63–7
- [83] Baek D H and Kim J 2017 MoS<sub>2</sub> gas sensor functionalized by Pd for the detection of hydrogen *Sensors Actuators B* **250** 686–91

- [84] Cho S Y, Koh H J, Yoo H W, Kim J S and Jung H T 2017 Tunable volatile-organic-compound sensor by using Au nanoparticle incorporation on MoS<sub>2</sub> *ACS Sens.* **2** 183
- [85] He X, Ying Z, Wen F, Li L and Wang G 2021 MoS<sub>2</sub>-doped spherical SnO<sub>2</sub> for SO<sub>2</sub> sensing under UV light at room temperature *Mater. Sci. Semicond. Process.* **134** 105997
- [86] Huo N, Yang S, Wei Z, Li S S, Xia J B and Li J 2014 Photoresponsive and gas sensing field-effect transistors based on multilayer WS<sub>2</sub> nanoflakes *Sci. Rep.* **4** 5209
- [87] Kuru C, Choi D, Kargar A, Liu C H, Yavuz S, Choi C, Jin S and Bandaru P R 2016 High-performance flexible hydrogen sensor made of WS<sub>2</sub> nanosheet-Pd nanoparticle composite film *Nanotechnology* **27** 195501
- [88] Jhk A, Amb C, Hwkc D and Sang S 2020 Flexible and low power CO gas sensor with Au-functionalized 2D WS<sub>2</sub> nanoflakes *Sensors Actuators B* **313** 128040
- [89] Qin Z, Chao O, Jian Z, Li W and Zeng D 2017 2D WS<sub>2</sub> nanosheets with TiO<sub>2</sub> quantum dots decoration for high-performance ammonia gas sensing at room temperature *Sensors Actuators B* **253** 1034–42
- [90] Ko K Y, Park K, Lee S, Kim Y, Woo W J, Kim D, Song J-G, Park J and Kim H 2018 Recovery improvement for large-area tungsten diselenide gas sensors *ACS Appl. Mater. Interfaces* **10** 23910–7
- [91] Chen Y A, Jx A, Cl A, Wei Z A, Xla B and Jza B 2021 Flexible NO<sub>2</sub> sensors based on WSe<sub>2</sub> nanosheets with bifunctional selectivity and superior sensitivity under UV activation *Sensors and Actuators B: Chemical* **333** 129571
- [92] Pan W, Zhang Y and Zhang D 2020 Self-assembly fabrication of titanium dioxide nanospheres-decorated tungsten diselenide hexagonal nanosheets for ethanol gas sensing application *Appl. Surf. Sci.* **527** 146781
- [93] Baek J, Yin D, Liu N, Omkaram I and Jung C 2016 A highly sensitive chemical gas detecting transistor based on highly crystalline CVD-grown MoSe<sub>2</sub> films *Nano Res.* **10** 2904
- [94] Chen X, Chen X, Han Y, Su C, Zeng M, Hu N, Su Y, Zhou Z, Wei H and Yang Z 2019 Two-dimensional MoSe(2) nanosheets via liquid-phase exfoliation for high-performance room temperature NO(2) gas sensors *Nanotechnology* **30** 445503
- [95] Zhang D, Li Q, Li P, Pang M and Luo Y 2019 Fabrication of Pd-Decorated MoSe<sub>2</sub> nanoflowers and density functional theory simulation toward ammonia sensing *IEEE Electron Device Lett.* **40** 616–9
- [96] Wu E, Yuan X, Yuan B, Hao Z, Hu X, Jing L and Zhang D 2018 Ultrasensitive and fully reversible NO<sub>2</sub> gas sensing based on p-type MoTe<sub>2</sub> under ultraviolet illumination *ACS Sens.* **3** 1719–26
- [97] Ming C, Li Z, Li W, Shan C, Li W, Li K, Gu G, Ye F, Zhong G H and Lei W 2018 Large-scale synthesis of single-crystalline self-standing SnSe<sub>2</sub> nanoplate arrays for wearable gas sensors *Nanotechnology* **29** 455501
- [98] Jiang T, Zhang T, He Q, Bi M, Chen X and Zhou X 2022 Adsorption performance and gas-sensing properties of V-GaSe to SF<sub>6</sub> decomposition components in gas-insulated switchgear *Appl. Surf. Sci.* **577** 151854
- [99] Zheng Z, Yao J D, Wang B and Yang G W 2017 Flexible, transparent and high-performance gas sensor based on layer-materials for wearable technology *Nanotechnology* **28** 415501
- [100] Kim S J, Koh H J, Ren C E, Kwon O and Jung H T 2018 Metallic Ti<sub>3</sub>C<sub>2</sub>T<sub>x</sub> MXene gas sensors with ultrahigh signal-to-noise ratio *ACS Nano* **12** 986–93
- [101] Lee E, Vahidmohammadi A, Yoon Y S, Beidaghi M and Kim D J 2019 Two-dimensional vanadium carbide MXene for gas sensors with ultrahigh sensitivity toward nonpolar gases *ACS Sens.* **6** 1603–11
- [102] Guo W, Surya S G, Babar V, Ming F and Salama K N 2020 Selective toluene detection with Mo<sub>2</sub>CT<sub>x</sub> MXene at room temperature *ACS Appl. Mater. Interfaces* **12** 57218–27
- [103] Abbas A N, Liu B, Chen L, Ma Y, Cong S, Aroonyadet N, Köpf M, Nilges T and Zhou C 2015 Black phosphorus gas sensors *ACS Nano* **9** 5618–24
- [104] Lee G, Kim S, Jung S, Jang S and Kim J 2017 Suspended black phosphorus nanosheet gas sensors *Sensors Actuators B* **250** 569–73
- [105] Miao J, Cai L, Zhang S, Nah J, Yeom J and Wang C 2017 Air-stable humidity sensor using few-layer black phosphorus *ACS Appl. Mater. Interfaces* **9** 10019–26
- [106] Mao J and Chen Y 2020 Strain-engineered black arsenene as a promising gas sensor for detecting SO<sub>2</sub> among SF<sub>6</sub> decompositions *Nanotechnology* **32** 065501
- [107] Yao J and Yang G 2021 Multielement 2D layered material photodetectors *Nanotechnology* **32** 3920018
- [108] Yao J and Yang G 2022 2D layered material alloys: synthesis and application in electronic and optoelectronic devices *Adv. Sci.* **9** 2103036
- [109] Feng Z H *et al* 2016 Chemical sensing by band modulation of a black phosphorus/molybdenum diselenide van der Waals hetero-structure *2D Mater.* **3** 035021
- [110] Liu L J, Ikram M, Ma L F, Zhang X Y, Lv H, Ullah M, Khan M, Yu H T and Shi K Y 2020 Edge-exposed MoS<sub>2</sub> nanospheres assembled with SnS<sub>2</sub> nanosheet to boost NO<sub>2</sub> gas sensing at room temperature *J. Hazard. Mater.* **393** 122325
- [111] Lee G, Kim S, Jung S, Jang S and Kim J 2019 Fabrication and characterization of a high-surface area MoS<sub>2</sub> @WS<sub>2</sub> heterojunction for the ultra- sensitive NO<sub>2</sub> detection at room temperature *J. Mater. Chem. A* **7** 14602–12
- [112] Kumar R, Dias W, Rubira R J G, Alaferdov A V, Vaz A R, Singh R K, Teixeira S R, Constantino C J L and Moshkalev S A 2018 Simple and fast approach for synthesis of reduced graphene oxide-MoS(2) hybrids for room temperature gas detection *IEEE Trans. Electron Devices* **65** 3943–9
- [113] Wang X Y, Gu D, Li X G, Lin S W, Zhao S H, Rumyantseva M N and Gaskov A M 2019 Reduced graphene oxide hybridized with WS<sub>2</sub> nanoflakes based heterojunctions for selective ammonia sensors at room temperature *Sensors Actuators B* **282** 290–9
- [114] Wang X Y, Huang B Y, Wu X F, Gu D and Li X G 2021 Enhanced ammonia sensing properties of rGO/WS<sub>2</sub> heterojunction based chemiresistive sensor by marginal sulfonate decoration *Sensors Actuators B* **337** 129776
- [115] Paolucci V, Emamjomeh S M, Ottaviano L and Cantalini C 2019 Near room temperature light-activated WS<sub>2</sub>-decorated rGO as NO<sub>2</sub> gas sensor *Sensors* **19** 2617
- [116] Choi H K *et al* 2017 Gas molecule sensing of van der Waals tunnel field effect transistors *Nanoscale* **9** 18644–50
- [117] Shi S, Hu R, Wu E, Li Q, Chen X, Guo W, Sun C, Hu X, Zhang D and Liu J 2018 Highly-sensitive gas sensor based on two-dimensional material field effect transistor *Nanotechnology* **29** 435502
- [118] Afzal A M, Iqbal M Z, Dastgeer G, Nazir G, Mumtaz S, Usman M and Eom J 2020 WS<sub>2</sub>/GeSe/WS<sub>2</sub> bipolar transistor-based chemical sensor with fast response and recovery times *ACS Appl. Mater. Interfaces* **12** 39524–32
- [119] Sun Q, Hao J Y, Zheng S L, Wan P, Li J L, Zhang D, Li Y Q, Wang T T and Wang Y 2020 2D/2D heterojunction of g-C<sub>3</sub>N<sub>4</sub>/SnS<sub>2</sub>: room-temperature sensing material for ultrasensitive and rapid-recoverable NO(2) detection *Nanotechnology* **31** 425502
- [120] Kuchi P S, Roshan H and Sheikhi M H 2020 A novel room temperature ethanol sensor based on PbS:SnS<sub>2</sub> nanocomposite with enhanced ethanol sensing properties *Journal of Alloys and Compounds* **816** 152666
- [121] Wu J, Wu Z X, Ding H J, Wei Y M, Huang W X, Yang X, Li Z Y, Qiu L and Wang X T 2020 Flexible, 3D

- SnS<sub>2</sub>/Reduced graphene oxide heterostructured NO<sub>2</sub> sensor *Sensors Actuators B* **305** 127445
- [122] Luo H *et al* 2021 Design of p–p heterojunctions based on CuO decorated WS<sub>2</sub> nanosheets for sensitive NH<sub>3</sub> gas sensing at room temperature *Nanotechnology* **32** 445502
- [123] Bae G, Song D S, Yi R L, Jeon I and An K S 2020 Chemical patterning of graphene via metal-assisted highly energetic electron irradiation for graphene homojunction-based gas sensors *ACS Appl. Mater. Interfaces* **12** 47802–10
- [124] Zheng W, Xu Y, Zheng L, Yang C, Pinna N, Liu X and Zhang J 2020 MoS<sub>2</sub> Van der Waals p–n junctions enabling highly selective room-temperature NO<sub>2</sub> sensor *Adv. Funct. Mater.* **30** 2000435
- [125] Ghosh S, Varghese A, Thakar K, Dhara S and Lodha S 2021 Enhanced responsivity and detectivity of fast WSe<sub>2</sub> phototransistor using electrostatically tunable in-plane lateral p–n homojunction *Nat. Commun.* **12** 3336
- [126] Lu J, Deng Z, Ye Q, Zheng Z, Yao J and Yang G 2021 Promoting the performance of 2D material photodetectors by dielectric engineering *Small Methods* **6** 2101046
- [127] Khan H *et al* 2017 Quasi physisorptive two dimensional tungsten oxide nanosheets with extraordinary sensitivity and selectivity to NO<sub>2</sub> *Nanoscale* **9** 19162–75
- [128] Liu W *et al* 2021 Ultrasensitive exhaled breath sensors based on anti-resonant hollow core fiber with *in situ* grown ZnO–Bi<sub>2</sub>O<sub>3</sub> nanosheets *Adv. Mater. Interfaces* **8** 2001978